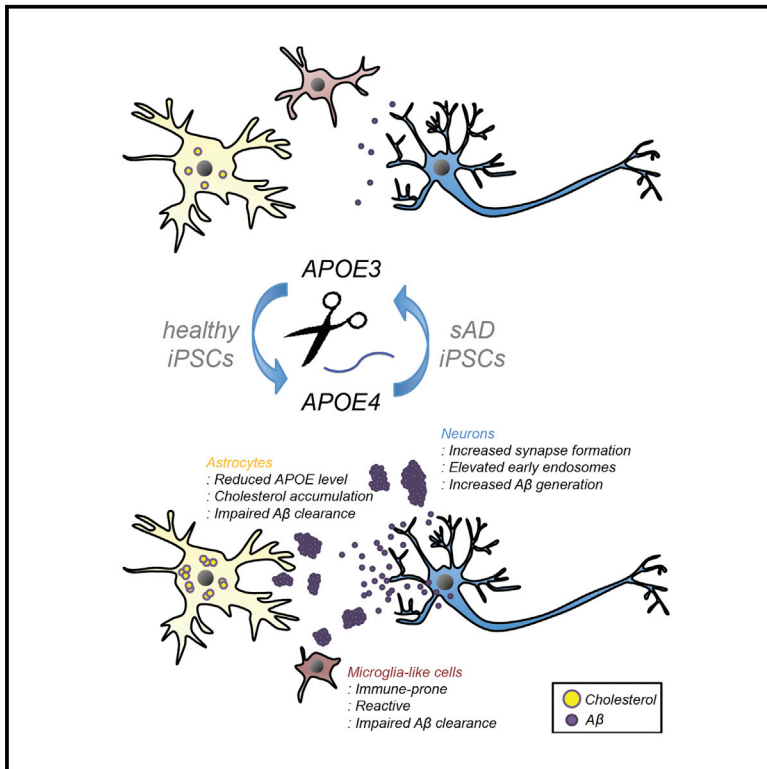APOE4 Causes Widespread Molecular and Cellular Alterations Associated with Alzheimer's Disease Phenotypes in Human iPSC-Derived Brain Cell Types

Graphical Abstract

Authors

Yuan-Ta Lin, Jinsoo Seo, Fan Gao, ..., Tak Ko, Bruce A. Yankner, Li-Huei Tsai

Correspondence

lhtsai@mit.edu

In Brief

By generating and characterizing isogenic *APOE3*- or *APOE4*-carrying human brain cell types, Lin et al. show that the *APOE4* variant can lead to extensive gene expression alterations, and multiple cellular phenotypes potentially related to AD pathogenesis, in neurons, astrocytes, and microglia.

Highlights

- The *APOE4* variant affected the transcriptional profile of induced neurons and glia

- Isogenic *APOE4* neurons exhibited early neuronal differentiation

- Isogenic *APOE4* glial cells were impaired in their ability to clear extracellular Aβ

- *APOE4* organoids displayed increased Aβ aggregates and hyperphosphorylation of tau

CellPress

APOE4 Causes Widespread Molecular and Cellular Alterations Associated with Alzheimer's Disease Phenotypes in Human iPSC-Derived Brain Cell Types

Yuan-Ta Lin,[1,2,6] Jinsoo Seo,[1,2,5,6] Fan Gao,[1] Heather M. Feldman,[3] Hsin-Lan Wen,[1] Jay Penney,[1,2] Hugh P. Cam,[1,2] Elizabeta Gjoneska,[1,2] Waseem K. Raja,[1,2] Jemmie Cheng,[1,2] Richard Rueda,[1] Oleg Kritskiy,[1] Fatema Abdurrob,[1] Zhuyu Peng,[1] Blerta Milo,[1] Chung Jong Yu,[1,2,4] Sara Elmsaouri,[1] Dilip Dey,[1] Tak Ko,[1] Bruce A. Yankner,[3] and Li-Huei Tsai[1,2,7,*]

[1]Picower Institute for Learning and Memory, Massachusetts Institute of Technology, Cambridge, MA 02139, USA
[2]Department of Brain and Cognitive Sciences, Massachusetts Institute of Technology, Cambridge, MA 02139, USA
[3]Department of Genetics, Harvard Medical School, Boston, MA 02115, USA
[4]Harvard University, John A. Paulson School of Engineering and Applied Sciences, Cambridge, MA 02139, USA
[5]Present address: Department of Brain and Cognitive Sciences, DGIST, Daegu 42988, Korea
[6]These authors contributed equally
[7]Lead Contact
*Correspondence: lhtsai@mit.edu
https://doi.org/10.1016/j.neuron.2018.05.008

SUMMARY

The apolipoprotein E4 (*APOE4*) variant is the single greatest genetic risk factor for sporadic Alzheimer's disease (sAD). However, the cell-type-specific functions of *APOE4* in relation to AD pathology remain understudied. Here, we utilize CRISPR/Cas9 and induced pluripotent stem cells (iPSCs) to examine *APOE4* effects on human brain cell types. Transcriptional profiling identified hundreds of differentially expressed genes in each cell type, with the most affected involving synaptic function (neurons), lipid metabolism (astrocytes), and immune response (microglia-like cells). *APOE4* neurons exhibited increased synapse number and elevated Aβ_{42} secretion relative to isogenic *APOE3* cells while *APOE4* astrocytes displayed impaired Aβ uptake and cholesterol accumulation. Notably, *APOE4* microglia-like cells exhibited altered morphologies, which correlated with reduced Aβ phagocytosis. Consistently, converting *APOE4* to *APOE3* in brain cell types from sAD iPSCs was sufficient to attenuate multiple AD-related pathologies. Our study establishes a reference for human cell-type-specific changes associated with the *APOE4* variant.

INTRODUCTION

Late-onset sporadic Alzheimer's disease (sAD) represents about 95% of all Alzheimer's disease cases (Alzheimer's Association, 2016). sAD etiology is likely due to complex interactions among different brain cell types leading to interconnected cellular pathologies (De Strooper and Karran, 2016). This dysfunction results in the pathological hallmarks of AD: senile plaques, neuro-

fibrillary tangles, neurodegeneration, and cognitive dysfunction (Canter et al., 2016). Critically important in the regulation of these processes is the balance between production and clearance of Aβ peptides from the brain. Aβ peptides, the main constituent of senile plaques, are produced mostly by neurons in an activity-dependent manner, and various astrocyte- and microglial-dependent mechanisms are thought to promote breakdown or clearance of Aβ from the brain (Bero et al., 2011; De Strooper and Karran, 2016). In contrast to the long-standing view of Alzheimer's as a neuron-centric disease, recent genetic studies have identified numerous non-neuronal genes as important risk factors for sAD (Lambert et al., 2013).

The earliest identified and most significantly associated genetic risk factor for sAD is the E4 allele of the *APOE*, which markedly increases AD risk relative to the *APOE3* allele, while the *APOE2* allele is considered protective (Corder et al., 1993; Lambert et al., 2013; Strittmatter et al., 1993). A single amino acid difference between APOE3 (Cys112) and APOE4 (Arg112) results in a protein conformational change that affects binding to apolipoprotein receptors, lipids, and Aβ (Liu et al., 2013). Brain APOE is mainly produced by astrocytes and secreted to the extracellular space, where it serves as the primary cholesterol carrier (Kim et al., 2009). Importantly, *APOE* is expressed by other brain cell types including neurons and microglia, where its expression can be altered under neuropathological conditions (Keren-Shaul et al., 2017; Mathys et al., 2017; Xu et al., 2006).

While the molecular etiology of AD driven by familial AD (fAD) mutations is relatively well understood, the specific impact of sAD risk factors including *APOE4* remains much less clear. Studies using mouse models expressing humanized *APOE* isoforms, cell lines, and postmortem human samples have revealed multiple AD-related pathological phenotypes impacted by *APOE4*, including reduced Aβ clearance, tauopathy, increased neuronal toxicity and mitochondrial dysfunction, though the cell-type-specific changes remain largely unexplored (Kim et al., 2009; Liu et al., 2013; Shi et al., 2017). However, findings
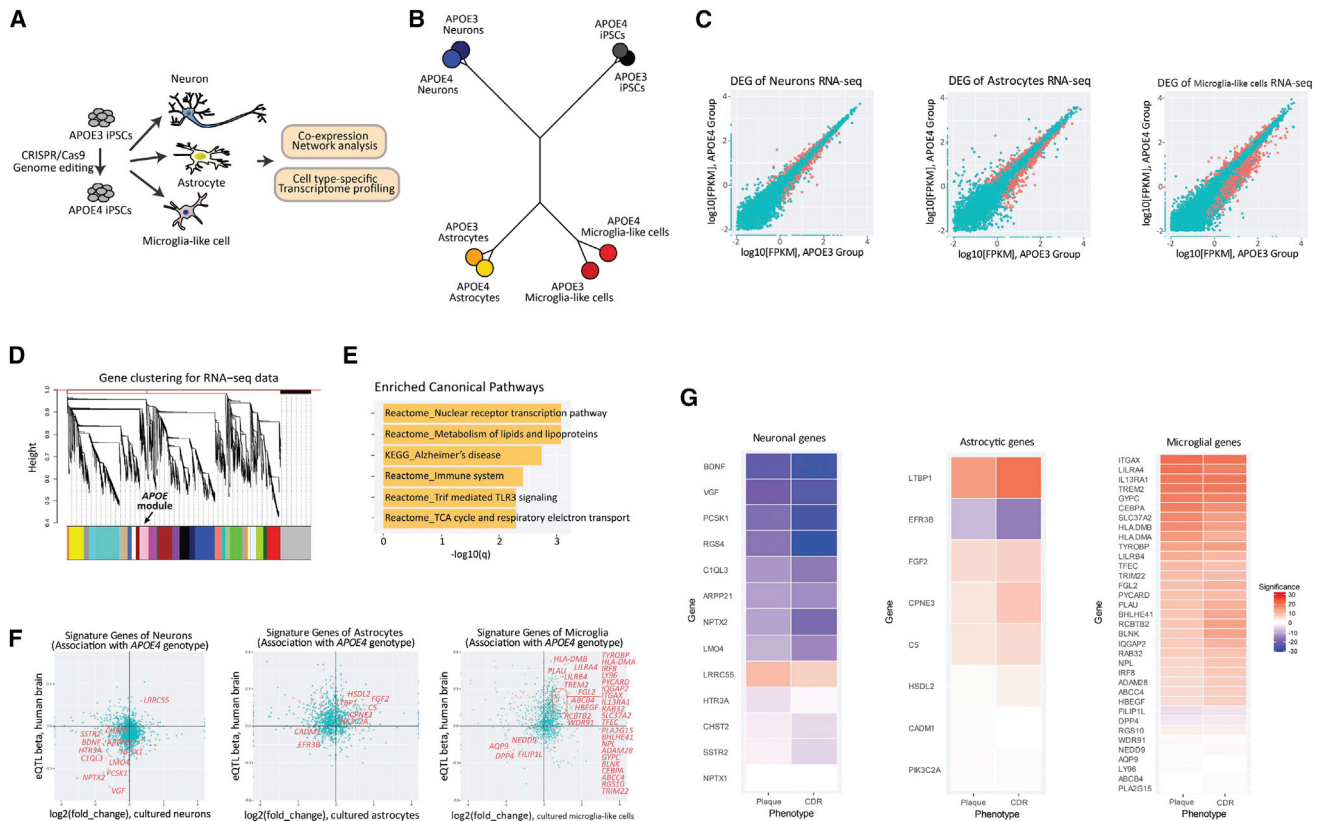
Figure 1. Altered Gene Expression in *APOE4* Neural and Glial Cells Is Correlated with Severe AD Clinical Phenotypes

(A) Schematics of RNA-seq with neurons, astrocytes, and microglia-like cells derived from isogenic iPSCs homozygous for either *APOE3* or *APOE4*.

(B) Phylogenetic dendrogram of RNA-seq data.

(C) Scatterplots of RNA-seq gene quantification values (log₁₀FPKM) of *APOE3* and *APOE4* groups in iPSC-derived brain cell types. DEGs are colored in red.

(D) Dendrogram of RNA-seq co-expression gene network visualizing clustering of gene expression patterns in iPSC-derived cells. Color bars indicate different gene modules, with *APOE* module colored in pink.

(E) Top six enriched canonical pathways of *APOE* gene module.

(F) Expression changes of cell-type signature genes in iPSC-derived corresponding *APOE4* cell types were compared to *APOE4* allele-associated eQTL effect sizes of those signature genes in postmortem human brain samples. The red dots in the plots showed overlap of significantly altered genes in both human brain samples and induced brain cell types. Among them, genes with concordant changes are pinpointed in the scatterplots.

(G) Expression of the concordant genes in control and MCI brains was correlated with two AD phenotypical measurements: neocortical plaque density and clinical dementia rating (CDR). Statistical p values of Spearman's correlation are visualized in heatmaps, with blue or red colors indicating negative or positive correlation.

from animal models are often hampered by concerns about translatability to humans due to species differences while studies using human cells are limited by accessibility to the relevant cell types and an inability to model complex disease *in vitro* (Calcoen et al., 2015). Recent advances in genome editing and differentiation protocols for generating 2D and 3D cultures from human induced pluripotent stem cells (iPSCs) now allow for a more systematic examination of *APOE4* effects on the different brain cell types in a human *in vitro* model (Paquet et al., 2016; Raja et al., 2016; Ran et al., 2013; Wang et al., 2018).

To better understand how *APOE4* affects major brain cell types involved in AD pathogenesis, we utilized CRISPR/Cas9 to create isogenic iPSC lines harboring homozygous *APOE4* alleles from unaffected parental *APOE3* cells. We found that *APOE4* iPSC-derived neurons, astrocytes, and microglia-like cells recapitulated phenotypes associated with AD at multiple

levels. The critical role for *APOE4* in AD pathogenesis is underscored by our observation that conversion of *APOE4* in sAD patient-derived iPSCs to *APOE3* was sufficient to alleviate most of the AD-related phenotypes observed in sAD iPSC-derived neurons, glia, and organoids.

RESULTS

Generating Isogenic Homozygous *APOE4* iPSCs

To enable systematic analysis of *APOE4* effects on specific brain cell types (Figure 1A), we used CRISPR/Cas9 gene editing to generate *APOE4* iPSCs from parental *APOE3* cells derived from an unaffected subject. Successful editing resulted in a Cys112Arg substitution in the APOE protein product, which was verified by Sanger sequencing of colonies derived from single putatively edited cells (Figure S1A; STAR Methods).

Whole-exome sequencing of our edited line as well as the parental iPSC line showed no unintended off-target mutations (Figures S1B–S1D), while karyotyping analysis revealed no chromosomal abnormalities in our isogenic lines (Figure S1E). Further, both parental and genome-edited iPSCs maintained comparable expression of pluripotency makers (Figure S1F).

Generation of Isogenic APOE iPSC-Derived Neurons, Astrocytes, and Microglia-like Cells

Next, we derived neurons, astrocytes, and microglia-like cells from our isogenic APOE3 and APOE4 iPSC lines. We generated neurons following the neurogenin2-mediated differentiation protocol (Zhang et al., 2013) with some modifications (Figure S2A; STAR Methods). To obtain a pure population, we cultured neurons supplemented with conditioned media from control human astrocytes, rather than co-culturing in direct contact with astrocytes. Although we cannot exclude potential effects on neurons by APOE proteins in the conditioned media released by APOE3 astrocytes, this approach allowed us to investigate the effect of neuronal APOE variation in human-induced neurons. To generate astrocytes, we derived iPSCs into neural progenitor cells (NPCs), which were subsequently induced to differentiate into astrocytes, while microglia-like cells were generated using a recently described protocol (Chen et al., 2014; Muffat et al., 2016) (Figures S2B and S2C; STAR Methods).

To obtain comprehensive transcriptional profiles of the three derived cell types, we next performed RNA sequencing (RNA-seq). Pairwise correlation of the transcriptomes showed segregation of iPSC-derived neurons, astrocytes, and microglia-like cells into their corresponding cell types regardless of APOE status (Figure 1B). The transcriptome signature of each cell type clustered with the corresponding cell type derived from either human brain samples or iPSCs reported by other groups (Figure S2D; STAR Methods), validating the identity of our iPSC-derived neural and glial cells.

APOE3 to APOE4 Switch Dramatically Alters Transcriptomes of iPSC-Derived Neurons and Glia

APOE variants were recently shown to affect gene expression in various cell types (Huang et al., 2017; Shi et al., 2017; Theendakara et al., 2016). We analyzed the effect of converting APOE3 to APOE4 on expression of genes in iPSCs and iPSC-derived neural and glial cells. We found many genes differentially regulated by APOE genotype in each cell type (Figure 1C), with iPSCs showing the lowest number of differentially expressed genes (DEGs) (Table S1). To identify genes whose expression is strongly correlated with APOE, we pooled all RNA-seq samples from all cell types of both genotypes and performed co-expression network analysis (STAR Methods). We found 857 genes with similar expression patterns to APOE (Figure 1D; Table S2). Gene ontology (GO) analysis indicated that expression of genes involved in lipid metabolism or immune responses, or associated with AD, was regulated synchronously with APOE (Figure 1E; Table S3). Considering the widespread effect of APOE4 on transcription, we asked whether DEGs observed in APOE4 cell types are regulated by a common set of transcription factors. Transcription motif analysis showed that, in addition to the three orphan motifs not associated with any known transcription factors, the motifs for nuclear factor 1 (NF1), activator protein 1 (AP-1), and nuclear factor kB (NF-kB) were markedly enriched in the promoters of genes in APOE module (Figure S2E). Among them, only the binding site for AP-1 was significantly enriched in DEGs affected by APOE4 in all of the induced brain cell types. We also performed microRNA (miRNA) motif analysis and found no common motifs in DEGs across the brain cell types and APOE co-regulated genes (Table S4).

We then asked whether altered gene transcription by the APOE4 variant in iPSC-derived brain cell types parallels APOE4-dependent changes in human brain samples. This analysis allows us to identify "gene hits" and related pathways, potentially representing perturbed biological processes driven by the APOE4 variant. We compared our datasets with those from 880 human brain samples (normal controls and mild cognitive impairment subjects; STAR Methods). We selected "signature" genes for each cell type, with enriched expression in neurons, astrocytes, or microglia based on a previous report (Zhang et al., 2016), and performed expression quantitative trait loci (eQTLs) analysis based on APOE4 genotype. These data were then compared to our RNA-seq results from each cell type. A significant number of neuronal signature genes exhibited concordant APOE genotype-dependent changes between the human samples and our iPSC-derived neurons (p = 0.042) (i.e., positively associated with APOE4 status in human and upregulated in APOE4 derived neurons, or vice versa). Among these coordinately regulated genes, more than half of them are known regulators of synaptic function (7 out of 12 genes, p = 2.59E−10), and most were negatively associated with APOE4 (Figure 1F). For astrocyte signature genes, eight genes were up- or downregulated based on APOE4 genotype in both human brain and iPSC-derived astrocytes (Figure 1F). Although this number of overlapping genes was not statistically significant (p = 0.23), it is interesting to note that three of those genes, PIK3C2A, CPNE3, and EFR3B, are known to be involved in phospholipid metabolic process (p = 5.39E−7). For microglia signature genes, there was a significant overlap between human brain and induced microglia-like cells (p = 1.6E−6) (Figure 1F). In contrast to neuronal signature genes, most of the microglia signature genes whose expression was affected by APOE4 in both human brain and microglia-like cells were upregulated. Strikingly, about half of them were associated with immune system process (p = 2.22E−9), suggesting that APOE4 impacts microglial functions related to the immune response. Expression of these APOE4-associated genes in each cell type showed significant negative or positive correlation with clinically defined AD phenotypes (neocortical plaque density and clinical dementia rating) in human patients (Figure 1G). Taken together, our transcriptome profiling showed that relative to APOE3, the APOE4 variant alters the expression of several pathways implicated in the development of AD in multiple brain cell types.

Increased Synapses, Early Endosomes, and Aβ42 Secretion in APOE4 Neurons

In the brain, neurons play an essential role in AD pathology as both the main producers of Aβ and the cell type most susceptible to damage. Despite this, the effect of neuronal APOE4 genotype on synaptic function and AD pathology is not clear.
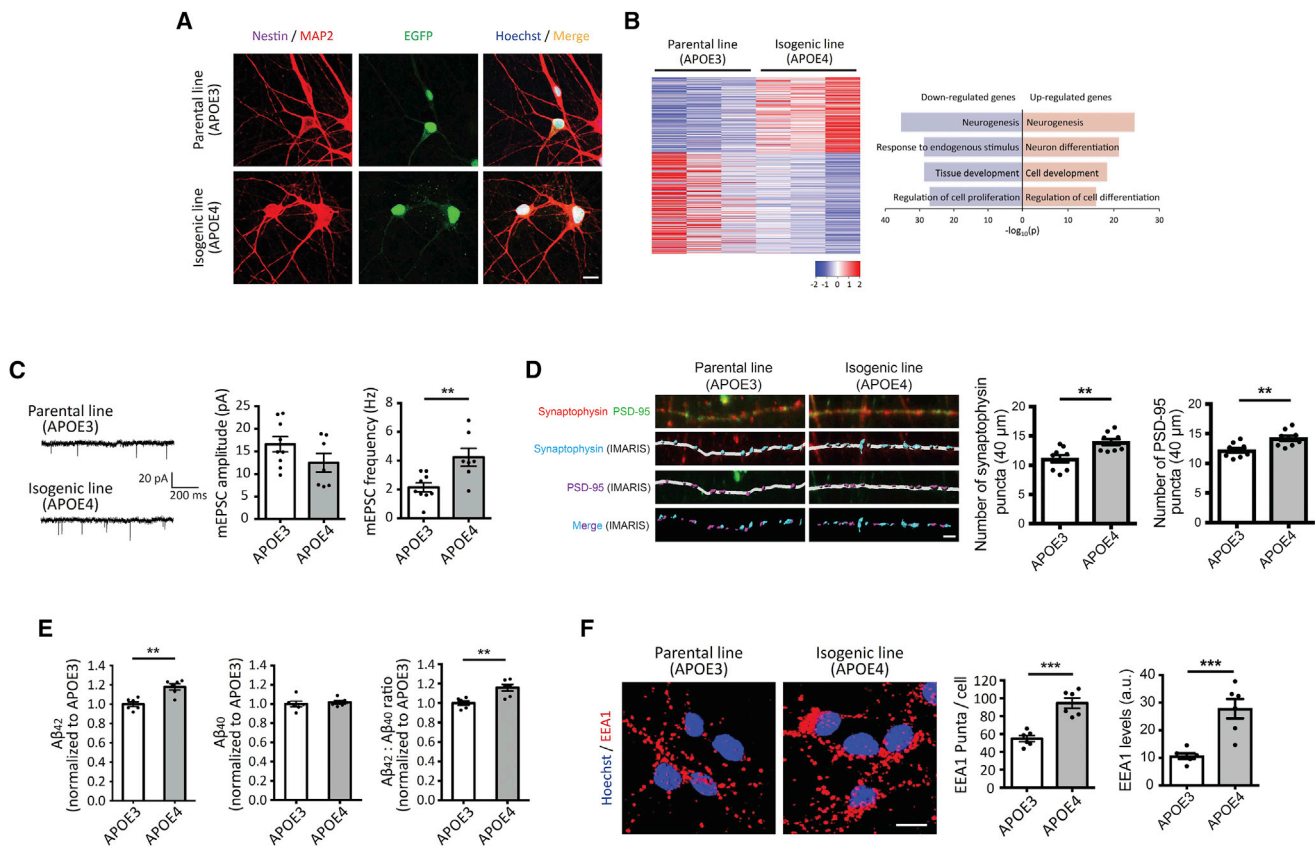
Figure 2. Increased Number of Synapses, Early Endosomes, and Aβ₄₂ Secretion in *APOE4* Neurons

(A) Immunocytochemistry with MAP2 and nestin antibodies in neurons. Scale bar, 10 μm.

(B) Heatmaps of *Z* score values and barplots of enriched GO terms for DEGs between *APOE3* and *APOE4* neurons.

(C) mEPSC amplitude and frequency in iPSC-derived neurons. Scale bar, 20 pA and 200 ms. n = 7∼9 from three independent cultures.

(D) Immunocytochemistry with synaptophysin and PSD-95 antibodies in neurons. Synaptophysin and PSD-95 signals were analyzed by IMARIS. n = 9 from four independent cultures. Scale bar, 2 μm.

(E) Secreted levels of Aβ₄₂ and Aβ₄₀ from iPSC-induced neurons were measured by ELISA and normalized to *APOE3* neurons. n = 6 per group.

(F) Immunocytochemistry with EEA1 antibody in neurons. Scale bar, 10 μm. n = 6 from three independent cultures. **p < 0.01, ***p < 0.001.

Error bars ± SEM.

Immunostaining results showed that neurons derived from both *APOE3* and *APOE4* iPSCs strongly expressed neuronal markers such as MAP2, but not neural progenitor markers such as nestin, after 4 weeks of induction (Figure 2A). RNA-seq revealed 445 genes that were significantly differentially expressed between *APOE3* and *APOE4* neurons (Figures 1E and 2B). GO analysis of these DEGs revealed that cell proliferation-related transcripts were downregulated by *APOE4*, whereas neuron differentiation-associated genes were upregulated (Figure 2B). To investigate the possibility of different synaptic activity between *APOE3*- and *APOE4*-carrying neurons, we performed intracellular recording on *APOE3* and *APOE4* neurons. We observed increased miniature excitatory postsynaptic current (mEPSC) frequencies with indistinguishable mEPSC amplitudes in *APOE4* neurons compared to *APOE3* controls (Figure 2C), suggesting increased release of neurotransmitter or elevated synaptic density in *APOE4* neurons. Consistent with the latter possibility, we observed an increase in number of synapses by immunostaining with the presynaptic marker, synaptophysin,

and the postsynaptic marker, PSD-95, in *APOE4* versus *APOE3* neurons (Figure 2D). Increased synaptic activity has been shown to correlate with increased Aβ production (Bero et al., 2011; Das et al., 2013). To determine whether *APOE4* neurons exhibit altered Aβ release, we measured the levels of Aβ secreted by *APOE3* and *APOE4* neurons by ELISA. Aβ₄₂ levels were 20% higher from *APOE4* cultures compared to *APOE3* cultures, although Aβ₄₀ levels were indistinguishable (Figure 2E).

In addition to elevated synaptic activity, endosomal abnormalities can elevate Aβ production by active cleavage of amyloid precursor protein (APP) via β-site APP-cleaving enzyme 1 (BACE1), generating β-CTF, a precursor of Aβ (Toh and Gleeson, 2016). Further, increased number and/or size of early endosomes has been described in the brains of AD patients (Cataldo et al., 2000). We examined early endosomes in neurons by immunostaining with an antibody against early endosome antigen 1 (EEA1). We found that the number of EEA1 puncta was higher in *APOE4* neurons compared to their *APOE3* counterparts. Total EEA1 levels, quantified as the product of "mean intensity of
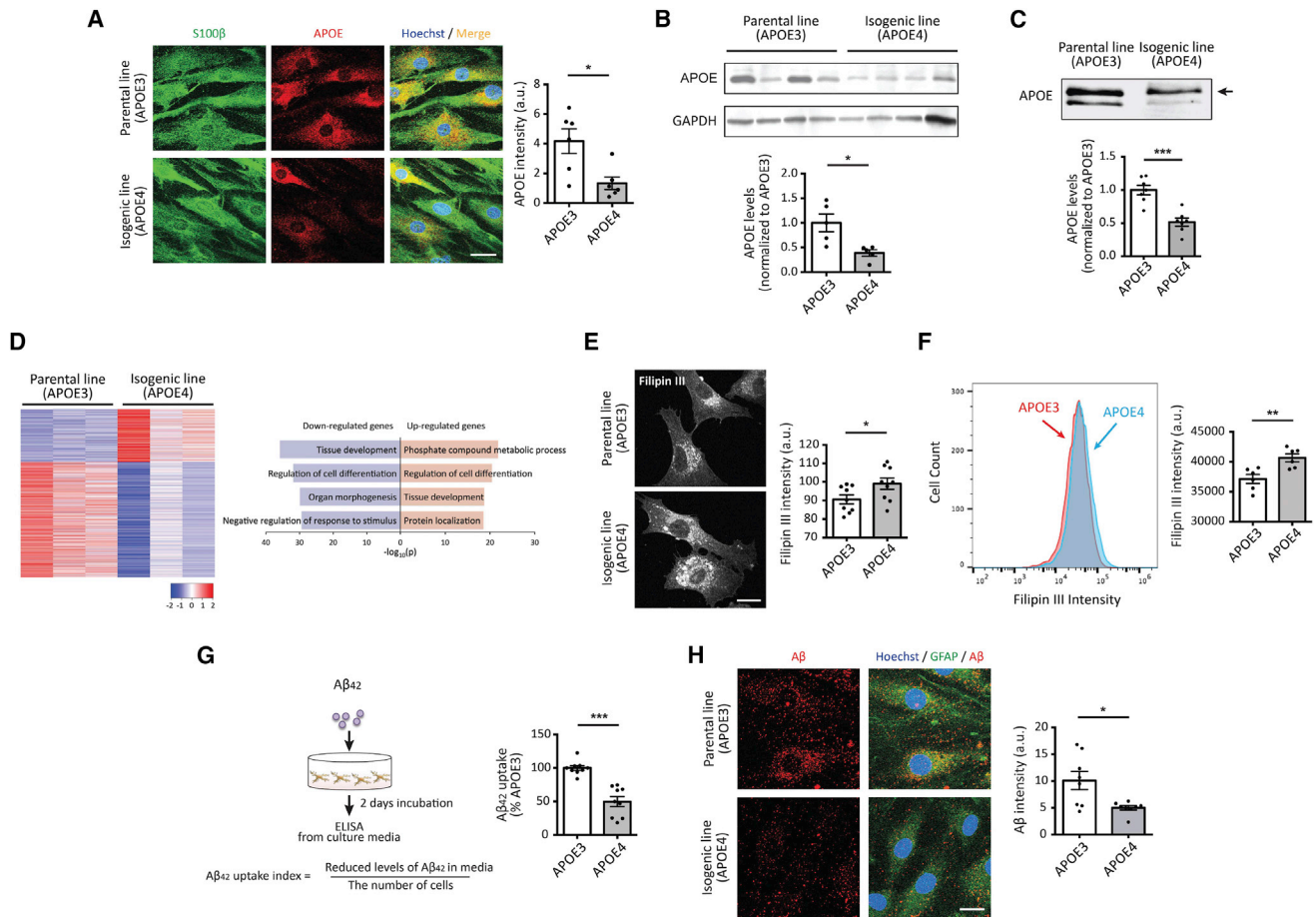
Figure 3. *APOE4* Astrocytes Exhibited Reduced APOE Protein Levels and Impaired Clearance of Extracellular Aβ$_{42}$

(A) Immunocytochemistry with APOE antibody in astrocytes homozygous for either *APOE3* or *APOE4*. Scale bar, 10 μm. n = 6 per group.

(B and C) Immunoblotting with APOE antibody in cell pellets (B) or cultured media (C) from *APOE3* or *APOE4* iPSC-induced astrocytes. Bar graphs represent relative immunoreactivity of APOE in each group normalized to *APOE3* genotype. n = 5∼7 per group. The upper bands (arrow) in (C) likely correspond to the sialiated form of APOE.

(D) Heatmaps of *Z* score values and barplots of enriched GO terms for DEGs between *APOE3* and *APOE4* astrocytes.

(E) iPSC-derived astrocytes were fixed and incubated with filipin III for 1 hr followed by imaging. The bar graph represents the intensity of filipin III in the images. Scale bar, 10 μm. n = 9 images from three independent cultures.

(F) iPSC-derived astrocytes were sorted based on the intensity of filipin III. The bar graph represents the intensity of filipin III in sorted cells. n = 6 per group.

(G) iPSC-derived astrocytes were incubated with Aβ$_{42}$ oligomers for 2 days, then residual Aβ$_{42}$ was measured by ELISA. Right: the Aβ$_{42}$ clearance index was calculated as described and normalized to *APOE3* astrocytes. n = 9 per group.

(H) Immunocytochemistry with Aβ and GFAP antibodies in astrocytes. Right: relative immunoreactivity of Aβ overlapped with GFAP in astrocytes. Scale bar, 10 μm. n = 8 images from three independent cultures. *p < 0.05, **p < 0.01, ***p < 0.001.

Error bars ± SEM.

signal" and "area covered by signal," were also increased in *APOE4* neurons (Figure 2F). These findings indicate that induced neurons harboring the *APOE4* allele exhibit disruption in pathways related to synaptic formation, associated with supernumerary synapses and increased frequency of synaptic transmission. Furthermore, *APOE4* neurons contain a greater number of early endosomes than *APOE3* controls.

APOE4 Astrocytes Exhibit Compromised Aβ Uptake

Astrocytes are the major source of secreted APOE, supplying lipids such as cholesterol to other cell types, including neurons, in the brain (Kim et al., 2009; Liu et al., 2013). Although astrocytes are known to have executive coordinating functions for neuronal activity and to play important protective roles in neurodegenerative disease (Sidoryk-Wegrzynowicz et al., 2011; Wyss-Coray et al., 2003), the effects of *APOE* genotype on astrocyte function remain incompletely understood. Immunostaining data showed that both *APOE3* and *APOE4* iPSC-derived astrocytes strongly express the astrocyte-specific marker S100β (Figure 3A). We examined APOE protein levels in these cells by immunostaining, finding significantly reduced APOE intensity in *APOE4* versus *APOE3* astrocytes (Figure 3A). Immunoblotting confirmed less APOE expression in astrocytes harboring the *APOE4* allele compared to *APOE3* astrocytes (Figure 3B). Similarly, there

was a reduction of secreted APOE in *APOE4* astrocytes cultures (Figure 3C). We then compared the transcriptomes of *APOE3* and *APOE4* astrocytes, noting that in parallel with reduced APOE protein, *APOE* transcription was also reduced by the *APOE4* genotype. In total, we found 1,327 DEGs (418 genes upregulated; 909 genes downregulated) in *APOE4* compared to *APOE3* astrocytes (Figures 1E and 3D). GO analysis indicated that genes related to tissue development were downregulated whereas phosphate-containing compound metabolic process-associated genes such as *CROT*, *LPGAT1*, and *PLPP3*, which are known to be involved in lipid metabolism, were upregulated in *APOE4* astrocytes (Figure 3D). Our transcriptome data further showed that the expression of numerous other genes with functions in lipid transport was decreased (Figure S3A).

Because one of the major functions of APOE is to transport lipids including cholesterol between cells, we explored whether *APOE4* astrocytes are impaired in cholesterol transport. We measured the cellular levels of cholesterol in *APOE3* and *APOE4* astrocytes by staining with filipin III, a compound known to fluoresce upon binding to cholesterol. We observed stronger signals of fluorescent filipin III in *APOE4* versus *APOE3* astrocytes (Figure 3E). We next used flow cytometry analysis to better quantify the filipin III signal in individual cells, finding higher average fluorescent intensity in *APOE4* compared to *APOE3* astrocytes (Figure 3F). We then examined levels of cholesterol in cultured media, including another isogenic clone of *APOE3 → APOE4* ($APOE4^{\#2}$) to control for possible variance among colonies. We observed increased levels of secreted cholesterol in both *APOE4* and $APOE4^{\#2}$ astrocyte cultures compared to those in *APOE3* cultures (Figure S3B), suggesting increased biosynthesis of cholesterol in *APOE4* astrocytes.

Astrocytes can uptake oligomeric and fibrillar $A\beta_{42}$ *in vitro* and *in vivo*, which contributes to Aβ clearance and prevents the detrimental effect of Aβ accumulation seen in AD (Koistinaho et al., 2004; Wyss-Coray et al., 2003). APOE forms lipoprotein complexes with various lipids including cholesterol, and it has been shown that APOE4-containing lipoproteins have impaired ability to bind and uptake extracellular Aβ, compared to those of APOE3 (Kim et al., 2009; Liu et al., 2013). However, it has not been directly or conclusively determined whether *APOE4* impacts the ability of astrocytes to uptake Aβ. To test this directly, we followed standard protocols by incubating iPSC-derived astrocytes with synthetic oligomeric $A\beta_{42}$ for 2 days to allow sufficient time for Aβ clearance (Wyss-Coray et al., 2003; STAR Methods). To quantify $A\beta_{42}$ uptake, we measured the fraction of oligomeric $A\beta_{42}$ removed from the media after the 2-day incubation (Figure 3G; STAR Methods). We confirmed that our astrocytes did not secrete any detectable amount of Aβ, ruling out endogenous Aβ as a contributing source to the media (data not shown). Also, Aβ treatment had no effect on cell viability or proliferation of *APOE3* or *APOE4* astrocytes (Figure S3C). *APOE4* astrocytes were notably less efficient than *APOE3* astrocytes in clearing $A\beta_{42}$ from the media (Figure 3G). In complementary experiments to directly measure $A\beta_{42}$ uptake by astrocytes, we performed immunostaining with antibodies against Aβ and the astrocyte marker GFAP. Data indicated that less $A\beta_{42}$ was taken up by *APOE4* astrocytes (Figure 3H). Since lysosomal activity can affect Aβ levels, we also examined lysosome-depen-

dent degradation of $A\beta_{42}$ by measuring intracellular Aβ with or without lysosomal inhibitors following $A\beta_{42}$ treatment. We observed increased $A\beta_{42}$ accumulation following lysosome inhibition in *APOE3* astrocytes compared to *APOE4* astrocytes, suggesting reduced lysosome-dependent $A\beta_{42}$ degradation in *APOE4* astrocytes (Figure S3D). Taken together, our results indicate that harboring the *APOE4* allele rather than *APOE3* negatively affects the expression of APOE, alters cholesterol metabolism, and impairs uptake of $A\beta_{42}$ in human iPSC-derived astrocytes.

APOE4 Microglia-like Cells Exhibit Inflammatory Gene Activation and Less Efficient $A\beta_{42}$ Uptake

Recent transcriptome analysis from human brain showed abundant expression of *APOE* in microglia (Gosselin et al., 2017); however, the potential effects of the *APOE4* variant on microglial gene expression and function are not known. Microglia, distinguished by their elaborated morphology reflecting their phagocytic function, are important mediators of inflammation in the nervous system. Recent genetic and functional studies have highlighted critical roles for microglia in brain health and disease, and identified dysfunction of this cell type as an important driver of sAD progression (Efthymiou and Goate, 2017; Keren-Shaul et al., 2017). Our iPSC-derived microglia-like cells clearly exhibit a ramified morphology characteristic of microglia (Muffat et al., 2016). Noticeably, in the course of generating microglia-like cells, we observed that those harboring the *APOE4* variant displayed fewer and shorter processes (Figure 4A). To gain further insights into potential effects of *APOE4* on this cell type, we compared the transcriptomes of *APOE3* and *APOE4* microglia-like cells. We found 1,460 DEGs in *APOE4* microglia-like cells compared to *APOE3* cells, more than in any other cell type we examined (Figures 1E and 4B). Interestingly, many more of the DEGs were downregulated (1,131 genes) than upregulated (329 genes) (Figure 4B, left panel). While downregulated genes were shown to be strongly associated with cell movement and development, a third of the 329 upregulated genes in *APOE4* microglia-like cells were associated with immune responses (Figure 4B, right panel; Figure S4A). These results suggest that *APOE4* likely renders microglia more prone to promote inflammation, and may also alter their phagocytic behavior. To explore the latter idea further, we examined the phagocytic activity of these cells toward Aβ. Since microglia take up Aβ much faster compared to astrocytes (Fu et al., 2012), we could monitor the uptake of fluorescently tagged $A\beta_{42}$ ($A\beta_{42}$-555) by microglia-like cells in real time. During the 1 hr imaging period, we found that microglia-like cells harboring the *APOE4* variant took up $A\beta_{42}$ much more slowly than *APOE3* cells (Figure 4C; Videos S1 and S2).

We recently showed that cerebral organoids generated from iPSC lines harboring fAD mutations such as *APP* duplication (APP^{DP}) or *PSEN1* mutation develop Aβ aggregates and hyperphosphorylated tau in 2–3 months (Raja et al., 2016). To investigate the ability of induced microglia-like cells to impact AD pathology in 3D organoid systems, we co-cultured *APOE3*- or *APOE4*-carrying microglia-like cells with 2-month-old APP^{DP} organoids that display Aβ aggregates. After 1 month of co-culture, we observed that similar numbers of microglia-like cells were incorporated into APP^{DP} organoids regardless of *APOE*
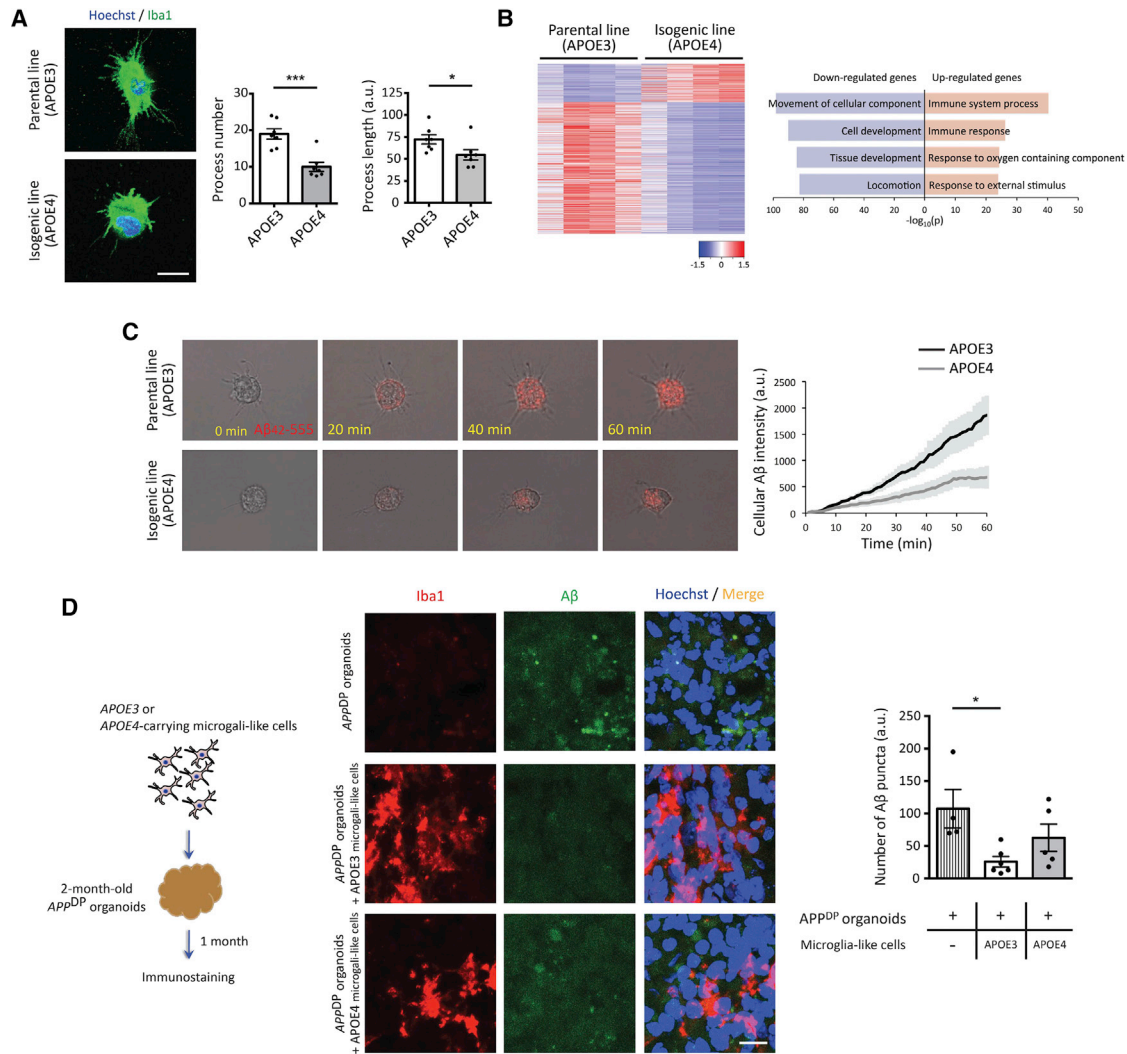
Figure 4. Altered Process Complexity and Impaired Clearance of Extracellular Aβ in *APOE4* Microglia-like Cells

(A) Immunocytochemistry with Iba1 antibody in *APOE3* or *APOE4* microglia-like cells. Bar graphs represent the number or length of process in microglia-like cells. Scale bar, 10 μm. n = 7 images from four independent cultures.

(B) Heatmaps of Z score values and barplots of enriched GO terms for DEGs between *APOE3* and *APOE4* microglia-like cells.

(C) Induced microglia-like cells were treated with Aβ$_{42}$-555, and its uptake was monitored under the microscope for 1 hr. Right: the intensity of cellular Aβ$_{42}$ in *APOE3* and *APOE4* microglia-like cells was plotted against time (min).

(D) Schematics to determine Aβ clearance in *APP^DP* organoids by microglia-like cells. Right: 3-month *APP^DP* organoids cultured without microglia-like cells or with either *APOE3* or *APOE4* microglia-like cells were fixed and subjected to immunostaining with Iba1 and Aβ antibodies. Bar graph represents the number of Aβ puncta. Scale bar, 10 μm. n = 4~6 organoids per group. *p < 0.05, ***p < 0.001.

Error bars ± SEM.

genotype (Figure S4B). However, unlike microglia-like cells (without Aβ treatment) in 2D-culture systems, *APOE4* microglia-like cells embedded in *APP^DP* organoids exhibited longer processes compared to *APOE3* cells, without a change in process number (Figures S4C and S4D). Shorter process length of microglia in AD brains has been shown to positively correlate with microglial Aβ uptake (Iaccarino et al., 2016; Sarlus and Heneka, 2017). Therefore, these data suggested that microglia-like cells with the *APOE4* variant may be less able to sense and respond to extracellular Aβ. We observed that Aβ accumulation

in organoids containing *APOE3* microglia-like cells was significantly less than that in *APP^DP* organoids without co-cultured microglia-like cells (Figure 4D). However, *APP^DP* organoids co-cultured with microglia-like cells carrying the *APOE4* allele exhibited more extracellular Aβ aggregates than those co-cultured with *APOE3* microglia-like cells (Figure 4D; Videos S3 and S4). Our data suggest that *APOE4* negatively impacts several aspects of microglial function that potentially hinder the ability of microglia to clear extracellular Aβ from AD brains, and may also influence the brain inflammatory profile.
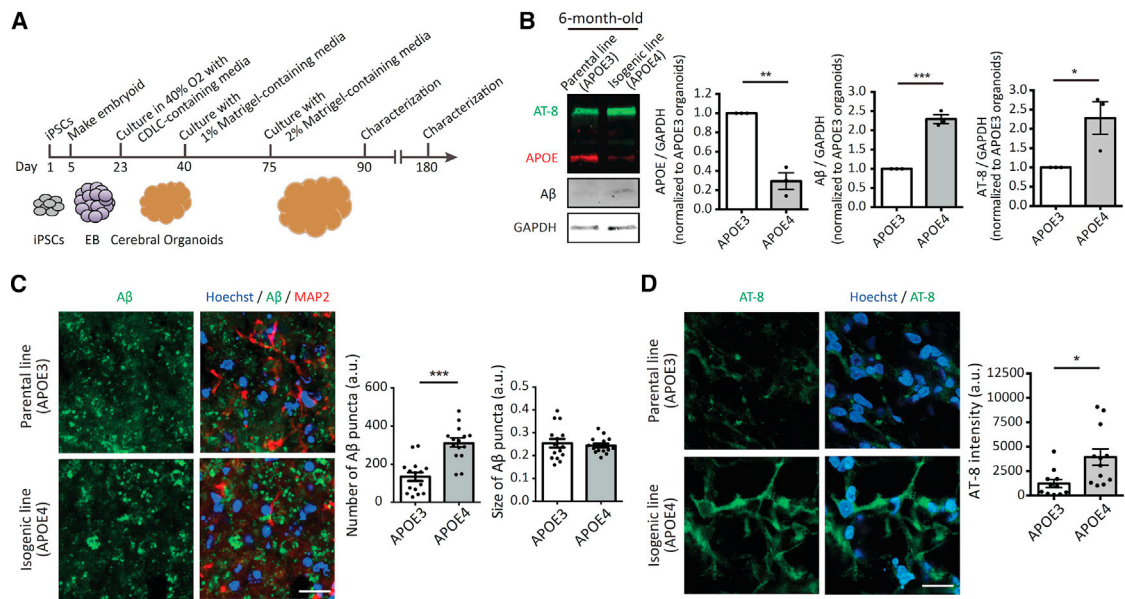
Figure 5. Increased Levels of Aβ and p-tau in *APOE4* iPSC-Derived Cerebral Organoids

(A) Schematics for generating cerebral organoids from iPSCs.

(B) Six-month organoids from *APOE3* or *APOE4* iPSCs were lysed and subjected to immunoblotting with APOE, Aβ, p-tau (AT-8), and GAPDH antibodies. Bar graphs represent relative immunoreactivity of APOE, Aβ, and AT-8 normalized to GAPDH. n = 3 per group.

(C and D) Six-month organoids from *APOE3* or *APOE4* iPSCs were fixed and subjected to immunostaining with Aβ, MAP2, and p-tau (AT-8) antibodies. Bar graphs represent the number and size of Aβ puncta (C) or immunoreactivity of AT-8 in organoids (D). Scale bar, 20 μm. n = 15 images from 5∼6 organoids. *p < 0.05, **p < 0.01, ***p < 0.001.

Error bars ± SEM.

APOE4 Organoids Accumulate Aβ and Exhibit Elevated Tau Phosphorylation

We next determined whether *APOE4* organoids would develop hallmarks of AD similar to fAD organoids as described above (Figure 5A). iPSCs used to generate organoids initially differentiate into NPCs and neurons, with astrocytes being detected at later time points (Quadrato et al., 2017). Thus, organoids serve initially as a 3D neuronal model and later as a model incorporating both neurons and astrocytes, which each exhibit *APOE4*-dependent defects as described above. We found that unlike fAD organoids, which developed Aβ aggregates after 2 months (Raja et al., 2016), *APOE4* organoids did not develop detectable Aβ accumulation by immunoblot assay at this time point (Figure S5A). Further, we found that APOE protein was undetectable in 3-month-old organoids, consistent with low expression of *APOE* in neurons, and few astrocytes at this stage of organoid development (Figure S5A). As expected, there was an increase in the number of GFAP-positive astrocytes by 6 months of age, in parallel with increased APOE protein levels (Figures 5B and S5B). We found that the levels of APOE protein in *APOE4* organoids were significantly lower compared to *APOE3* organoids (Figure 5B); both had a similar number of total astrocytes at this stage (Figure S5B). Remarkably, 6-month-old *APOE4* organoids exhibited increased Aβ accumulation and tau phosphorylation (p-S202/T205) compared to *APOE3* organoids (Figure 5B). Immunostaining further demonstrated an increased number of Aβ aggregates and elevated p-tau levels in 6-month-old *APOE4* organoids compared to their *APOE3* counterparts (Figures 5C and 5D).

Taken together, these data indicate that while *APOE4* organoids exhibit delayed development of AD pathology relative to fAD organoids, the *APOE4* variant alone is sufficient to cause AD hallmarks in cerebral organoids.

Converting *APOE4* to *APOE3* Attenuates AD-Related Phenotypes in Neurons, Glia, and Organoids Derived from sAD iPSCs

Because *APOE4* carries the highest known risk for sAD, we next tested whether converting *APOE4* in iPSCs from an sAD patient to *APOE3* was sufficient to ameliorate the molecular and cellular phenotypes of various iPSC-derived brain cell types we have uncovered. We used a similar CRISPR/Cas9 approach as described above to create isogenic iPSCs homozygous for *APOE3* from sAD iPSCs homozygous for *APOE4* (Figure S6A; STAR Methods). Karyotyping analysis confirmed that there were no detectable chromosomal rearrangements in these isogenic lines (Figure S6B). Whole-exome sequencing identified, other than the expected *APOE4* to *APOE3* change, a single variant in the *TRIOBP* gene causing replacement of Ala with Val (Figures S6C and S6D). TRIOBP is a TRIO and F-actin-binding protein that is known to be involved in actin cytoskeleton organization (Seipel et al., 2001). While mutations of *TRIOBP* have been associated with autosomal recessive nonsyndromic deafness (Shahin et al., 2006), there is no known link of *TRIOBP* with AD or any other neurodegenerative diseases. We then generated neurons, astrocytes, microglia-like cells, and organoids from these two iPSC lines.
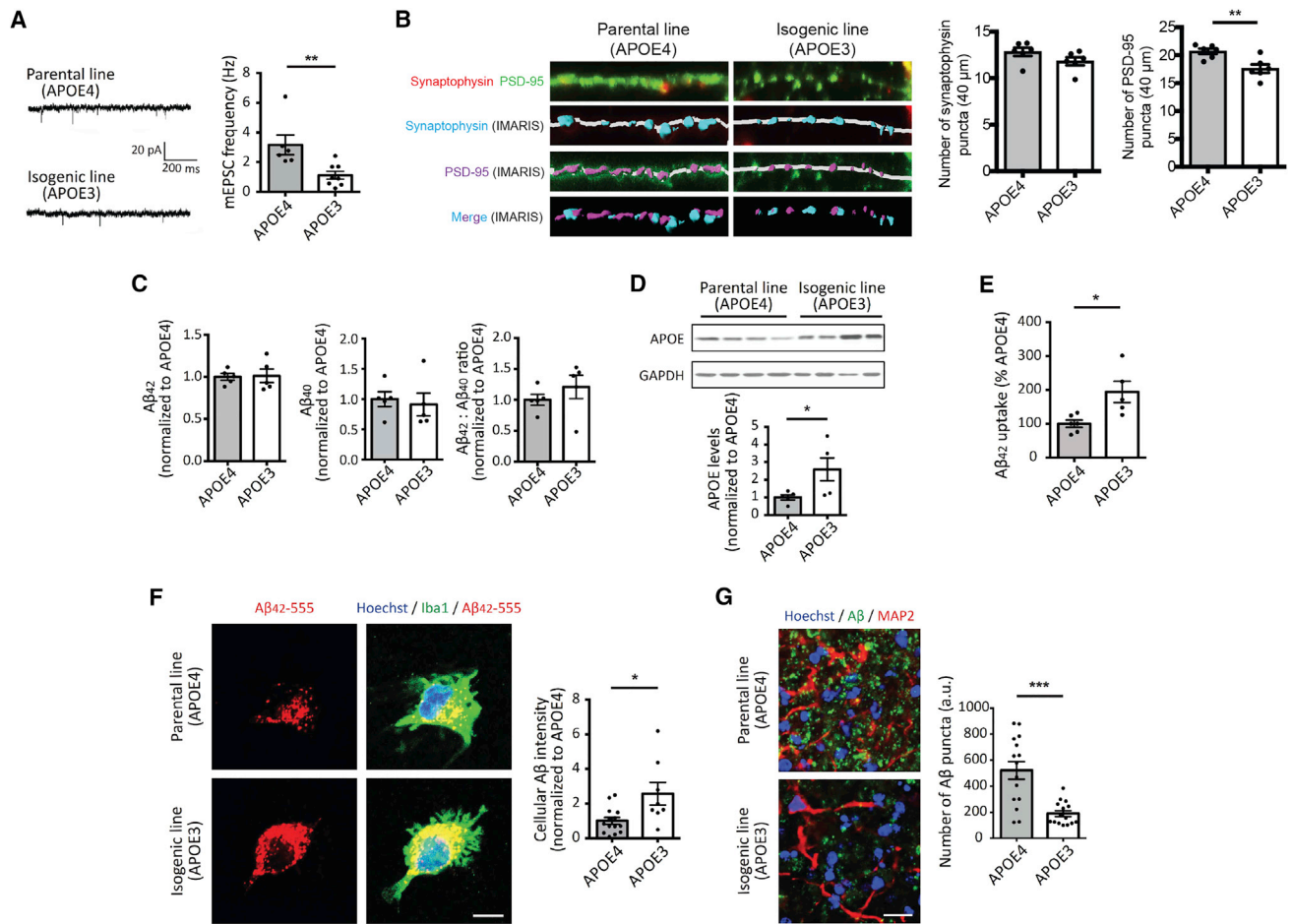
Figure 6. Converting *APOE4* to *APOE3* Attenuates AD-Related Phenotypes in sAD iPSC-Derived Neurons, Glia, and Organoids

(A) mEPSC frequency (right) in iPSC-derived neurons from *APOE4* or *APOE3* iPSCs. Scale bar, 20 pA and 200 ms. n = 6∼8 from three independent cultures.

(B) Immunocytochemistry with synaptophysin and PSD-95 antibodies in neurons derived from *APOE4* or *APOE3* iPSCs. Synaptophysin and PSD-95 signals were analyzed by IMARIS. Scale bar, 2 μm. n = 6 from three independent cultures.

(C) Secreted levels of $A\beta_{42}$ and $A\beta_{40}$ from iPSC-induced neurons were measured by ELISA and normalized to *APOE4* neurons. n = 5 per group.

(D) Relative immunoreactivity of APOE in induced *APOE4* or *APOE3* astrocytes was normalized to *APOE4* astrocytes. n = 5 per group.

(E) iPSC-derived astrocytes were incubated with $A\beta_{42}$ oligomers for 2 days, then residual $A\beta_{42}$ was measured by ELISA. The $A\beta_{42}$ clearance index was calculated and normalized to *APOE4* astrocytes. n = 5∼6 per group.

(F) Immunocytochemistry with $A\beta$ and Iba1 antibodies in *APOE3* or *APOE4* microglia-like cells. Right: relative immunoreactivity of $A\beta$ overlapped with Iba1 was normalized to that of *APOE4* microglia-like cells. Scale bar, 5 μm. n = 8∼14 images from four independent cultures.

(G) Six-month organoids from *APOE4* or *APOE3* iPSCs were subjected to immunostaining with $A\beta$ and MAP2 antibodies. The bar graph represents the number of $A\beta$ puncta in organoids. Scale bar, 20 μm. n = 15 images from 5∼6 organoids. *p < 0.05, **p < 0.01, ***p < 0.001.

Error bars ± SEM.

We first characterized induced neurons and found that *APOE3* neurons exhibited reduced mEPSC frequencies and fewer synapses compared to *APOE4* neurons (Figures 6A and 6B). However, we did not observe a significant difference in the levels of secreted $A\beta_{42}$ or $A\beta_{40}$ (Figure 6C) between the two groups. Also, while converting *APOE4* to *APOE3* appeared to reduce the number of early endosomes in neurons, the effect did not reach significance (p = 0.06; Figure S6E). In induced astrocytes, we found higher APOE protein levels and less accumulation of intracellular cholesterol in *APOE3* than *APOE4* astrocytes (Figures 6D, S6F, and S6G). Moreover,

converting *APOE4* to *APOE3* enhanced the ability of astrocytes and microglia-like cells to uptake extracellular $A\beta$ (Figures 6E and 6F). We also addressed the contribution of the *APOE4* variant to $A\beta$ accumulation in sAD cerebral organoids and found that after 6 months of culture, *APOE3* organoids displayed less $A\beta$ compared to age-matched *APOE4* organoids (Figure 6G). Overall, these results indicate that most of the AD-related phenotypes observed in *APOE4* iPSC-derived brain cell types and organoids could be reversed by editing to *APOE3*, confirming the central role of *APOE4* in sAD pathology.

DISCUSSION

Early Maturation of *APOE4* Neurons

Our transcriptional analysis revealed roughly equal numbers of up- and downregulated genes in iPSC-derived neurons. GO analysis showed that the expression of genes related to neuronal differentiation was upregulated by *APOE4*. Consistently, the increase in mEPSC frequency and number of synapses we observed in *APOE4* neurons is suggestive of enhanced neuronal differentiation/maturation. We observed similar increases in synapse numbers in *PSEN1 M146I* iPSC-derived neurons (data not shown), indicating that early neuronal maturation could be a common phenotype of neurons with AD-linked mutations.

Neuronal signature genes whose expression was correlated with *APOE4* genotype in both human and iPSC-derived samples were mostly downregulated and associated with synaptic functions (Figures 1F and 1G). One of the significantly downregulated genes, *BDNF*, was shown to have reduced expression in human *APOE4* carriers, which paralleled cognitive impairment (Liu et al., 2015; Alvarez et al., 2016). Our analysis of exome sequencing data from AD patients and unaffected controls showed a strong association between a SNP in the *BDNF* gene (E6K) with neocortical plaque density (Figure S2F; STAR Methods), although whether this SNP leads to loss of function remains to be clarified. Furthermore, elevating BDNF in the brains of AD rodent models also attenuated AD-related pathology (Zhang et al., 2015). Thus, BDNF is a promising candidate that could account for some of the observed *APOE4* neuronal phenotypes.

Our motif analysis identified high enrichment for transcriptional activator AP-1-binding sites in promoters of genes within the *APOE* module from human brain, and DEGs affected by *APOE4* in our induced brain cells (Figure S2E). It was recently shown that E4 was the most potent APOE isoform in eliciting AP-1 activation in neurons (Huang et al., 2017). Our analysis suggests that *APOE4*-dependent effects on AP-1 activation are not restricted to neurons, though further study will be required to determine whether common or distinct regulatory pathways operate in each cell type, and whether these mechanisms could be targeted for therapeutic development.

APOE4 Effects on Astrocytes

We found that the levels of APOE protein and mRNA were reduced in *APOE4* astrocytes, suggesting that the *APOE4* variant can negatively impact its own transcription. Consistently, studies from both humans and mouse models have reported similar reductions in APOE4 protein relative to APOE3 (Mooijaart et al., 2006; Shi et al., 2017). In contrast, a recent study of iPSC-derived astrocytes showed similar APOE levels in *APOE3* versus *APOE4* cells; however, these findings may be confounded by the use of non-isogenic backgrounds (Zhao et al., 2017). Interestingly, we found that the reduced *APOE4* mRNA and protein levels in iPSC-derived cell types were specific to astrocytes (data not shown), indicating the effect is cell-type specific.

Our gene expression analyses indicated the *APOE4* variant regulates expression of numerous lipid metabolism and transport genes (Figures 1E, 1F, 3D, and S3A). One of the intriguing phenotypes we found was the accumulation of intracellular and extracellular cholesterol in *APOE4* astrocyte cultures.

Cholesterol and other lipids are crucial for a wide range of cellular functions in the brain, and altered metabolism or transport appears to be associated with multiple pathological phenotypes in various neurodegenerative disorders (Göritz et al., 2002; Mauch et al., 2001). Remarkably, the *APOE4* variant appears to regulate both the metabolism and transport of lipids such as cholesterol, with potential effects on each of the three brain cell types. For instance, cholesterol-rich lipid rafts serve as a platform for APP processing to Aβ (Cheng et al., 2007), increased cholesterol can result in enlarged early endosomes (Marquer et al., 2014), and altered cholesterol levels can affect gene expression (Goldstein et al., 2006). Therefore, additional experiments from each of the *APOE4* brain cell types have the potential to yield important insights into these aspects of APOE biology.

Importantly, we also found that *APOE4* astrocytes were less efficient in uptake and clearance of Aβ compared to their *APOE3* counterparts. APOE4 is known to form smaller lipoprotein complexes with reduced affinity for Aβ, as well as for APOE receptors, compared to APOE3 (Kim et al., 2009). Combined with reduced astrocyte APOE4 protein expression, these factors would be predicted to strongly impair Aβ clearance by astrocytes and other cell types. However, the role of APOE itself in Aβ clearance remains contentious; some *in vivo* studies have shown that APOE is required for Aβ clearance, while others have observed increased extracellular Aβ clearance and attenuation of tauopathy in the absence of APOE (Holtzman et al., 1999; Koistinaho et al., 2004; Liao et al., 2014a; Shi et al., 2017). Further work will be required to clarify this issue, as well as to determine whether the deficit in Aβ uptake by *APOE4* astrocytes is due solely to differences in levels and function of secreted APOE4 versus APOE3 protein, or if unrelated deficits in cellular function are more important.

Impaired Aβ Uptake and Inflammatory Alterations in *APOE4* Microglia-like Cells

In support of cell-intrinsic *APOE4*-dependent deficits in Aβ uptake, we found that *APOE4* microglia-like cells also exhibited reduced Aβ uptake relative to their *APOE3* counterparts, despite internalizing Aβ much more quickly than astrocytes (1 hr for microglia-like cells in Figure 4C compared to 2 days for astrocytes in Figure 3H). We further found that *APOE4* microglia-like cells exhibited altered morphologies compared to *APOE3* cells. In 2D culture (without Aβ treatment), *APOE4* microglia-like cells had fewer and shorter processes, while after embedding in 3D neuronal cultures (that produce Aβ), the same cells had longer processes than their *APOE3* counterparts. These observations are consistent with impairment in the ability of *APOE4* microglia-like cells to effectively sense and/or respond to Aβ in their environment. Given the importance of microglia surveillance and response functions to brain health, such impairment could have considerable detrimental effect for *APOE4* carriers (Salter and Beggs, 2014).

Multiple studies show a positive relationship between upregulation of immune-related genes and *APOE4* genotype (Keren-Shaul et al., 2017; Mathys et al., 2017). Our study suggests that carrying the *APOE4* variant could be sufficient to convert resting microglia into immune-active. This alteration likely associates with morphological changes and may underlie

the observed alterations in Aβ uptake. It will be important to determine whether redirecting these cells from a "reactive" to a "homeostatic" state could restore their Aβ uptake ability.

Among the upregulated immune genes we observed in *APOE4* microglia-like cells was *IRF8*, which was shown to induce transcription of many immune-related genes and transform microglia into a reactive state (Masuda et al., 2012). Thus, we asked whether the immune-related transcriptional changes in *APOE4* microglia-like cells could be mediated via IRF8. Using available IRF8 chromatin immunoprecipitation sequencing (ChIP-seq) data from mouse bone marrow (Olsson et al., 2016), we observed that upregulated genes indeed had higher IRF8 signals, consistent with an important role for this protein in *APOE4*-related transcriptional changes (Figure S4E). Interestingly, we also observed that expression of *TREM2* (and its signaling adaptor *TYROBP*), which is crucial for microglial function and is itself a highly significant AD risk gene (Ulrich and Holtzman, 2016), was positively correlated with *APOE4* genotype (Figures 1F and S4F). This is consistent with recent studies showing increased levels of soluble TREM2 in cerebrospinal fluid of AD patients (Heslegrave et al., 2016); however, the mechanisms by which *TREM2* and *TYROBP* are regulated by *APOE* variants will require further investigation.

Late Onset of Amyloid Accumulation in *APOE4* Organoids Compared to fAD Organoids

Increased levels of Aβ and p-tau in *APOE4* versus *APOE3* organoids were apparent after 6 months of culture, which is relatively delayed compared to 2 months of culture for organoids with fAD mutations (Raja et al., 2016). We observed an increased number of synapses and early endosomes in *APOE4* neurons, which could contribute to elevated Aβ generation; however, the increase of Aβ42 secretion by *APOE4* versus *APOE3* neurons is much less than the 3-fold increase reported in fAD neurons versus controls (Paquet et al., 2016). Astrocyte abundance in organoids also increases with duration of culture (Quadrato et al., 2017), consistent with our ability to detect APOE protein at 6 month of culture, but not at 3 months (Figure 4B). Thus, both moderate increases of Aβ secretion by neurons and impaired Aβ clearance by astrocytes could contribute to Aβ accumulation in *APOE4* organoids at 6 months of age.

Amelioration of AD-Related Phenotypes by Switching *APOE4* to *APOE3*

To complement our studies of *APOE4*-dependent defects in brain cell types, we edited the *APOE4* allele of iPSCs derived from an sAD patient to *APOE3*. We were able to reverse most of the AD-associated phenotypes we examined by this *APOE4* to *APOE3* conversion, underscoring the critical importance of this genetic variant. However, we did not see a reduction in Aβ42 secretion from *APOE3* versus *APOE4* sAD neurons (Figure 6D). Similarly, the reduction in early endosome numbers in *APOE3* sAD neurons was not statistically significant, although there was a trend compared to *APOE4* sAD neurons (Figure 6E). It is likely that additional factors in this sAD iPSC-derived cell line confound the AD-related pathologies we observe.

The *APOE2* allele, which has been suggested to have a protective effect on the onset of AD, is also of great interest. However, compared to the *APOE4* variant, our knowledge of the cellular and molecular alterations associated with *APOE2* is quite limited. As such, it is not clear whether the effects of the *APOE2* allele would be completely opposite to those of *APOE4* on the examined cell types and organoids. Investigating the nature of protective effects of *APOE2* on AD pathology using the human iPSC model systems warrants further study.

In summary, our study suggests that *APOE4* impacts AD pathology mainly through impairment of astrocyte- and microglia-mediated Aβ clearance. Moreover, there are notable abnormalities associated with lipid metabolism in *APOE4* astrocytes and potentially microglia. In this regard, targeting glia-mediated Aβ clearance and lipid biogenesis/metabolism could be potential targets for therapeutic intervention. Furthermore, determining whether *APOE4* mutation results in loss of functions or gain of toxic functions will be critical to tailor appropriate therapeutic interventions for *APOE4* carriers. Our human *APOE* isogenic iPSCs offer a powerful set of useful tools to address these important questions.

STAR★METHODS

Detailed methods are provided in the online version of this paper and include the following:

- KEY RESOURCES TABLE
- CONTACT FOR REAGENT AND RESOURCE SHARING
- EXPERIMENTAL MODEL AND SUBJECT DETAILS
  - Human induced-pluripotent stem cells
- METHOD DETAILS
  - Generation of isogenic iPSC lines
  - Differentiation of iPSCs into neurons
  - Differentiation of iPSCs into astrocytes
  - Generation of induced microglia-like cells
  - Organoids culture
  - Bioinformatics
  - Immunoblot analysis
  - Immunostaining analysis
  - Electrophysiology
  - Synaptophysin puncta quantification in iPSC-derived neurons
  - Measurement of secreted Aβ levels in iPSC-derived neurons by ELISA
  - Cholesterol assay
  - Microscopy
  - Aβ42 uptake assay
  - Lysosomal inhibitors treatment in iPSC-derived astrocytes
- QUANTIFICATION AND STATISTICAL ANALYSIS
  - Statistical analyses
- DATA AND SOFTWARE AVAILABILITY

REFERENCES

Alvarez, X.A., Alvarez, I., Iglesias, O., Crespo, I., Figueroa, J., Aleixandre, M., Linares, C., Granizo, E., Garcia-Fantini, M., Marey, J., et al. (2016). Synergistic increase of serum BDNF in Alzheimer patients treated with cerebrolysin and donepezil: association with cognitive improvement in ApoE4 cases. Int. J. Neuropsychopharmacol. 12, 1–10.

Alzheimer's Association (2016). 2016 Alzheimer's disease facts and figures. Alzheimers Dement. 12, 459–509.

Bero, A.W., Yan, P., Roh, J.H., Cirrito, J.R., Stewart, F.R., Raichle, M.E., Lee, J.-M., and Holtzman, D.M. (2011). Neuronal activity regulates the regional vulnerability to amyloid-β deposition. Nat. Neurosci. 14, 750–756.

Busskamp, V., Lewis, N.E., Guye, P., Ng, A.H.M., Shipman, S.L., Byrne, S.M., Sanjana, N.E., Murn, J., Li, Y., Li, S., et al. (2014). Rapid neurogenesis through transcriptional activation in human stem cells. Mol. Syst. Biol. 10, 760.

Calcoen, D., Elias, L., and Yu, X. (2015). What does it take to produce a breakthrough drug? Nat. Rev. Drug Discov. 14, 161–162.

Canter, R.G., Penney, J., and Tsai, L.H. (2016). The road to restoring neural circuits for the treatment of Alzheimer's disease. Nature 539, 187–196.

Cataldo, A.M., Peterhoff, C.M., Troncoso, J.C., Gomez-Isla, T., Hyman, B.T., and Nixon, R.A. (2000). Endocytic pathway abnormalities precede amyloid beta deposition in sporadic Alzheimer's disease and Down syndrome: differential effects of APOE genotype and presenilin mutations. Am. J. Pathol. 157, 277–286.

Chen, J., Bardes, E.E., Aronow, B.J., and Jegga, A.G. (2009). ToppGene Suite for gene list enrichment analysis and candidate gene prioritization. Nucleic Acids Res. 37, W305-11.

Chen, C., Jiang, P., Xue, H., Peterson, S.E., Tran, H.T., McCann, A.E., Parast, M.M., Li, S., Pleasure, D.E., Laurent, L.C., et al. (2014). Role of astroglia in Down's syndrome revealed by patient-derived human-induced pluripotent stem cells. Nat. Commun. 5, 4430.

Cheng, H., Vetrivel, K.S., Gong, P., Meckler, X., Parent, A., and Thinakaran, G. (2007). Mechanisms of disease: new therapeutic strategies for Alzheimer's disease—targeting APP processing in lipid rafts. Nat. Clin. Pract. Neurol. 3, 374–382.

Corder, E.H., Saunders, A.M., Strittmatter, W.J., Schmechel, D.E., Gaskell, P.C., Small, G.W., Roses, A.D., Haines, J.L., and Pericak-Vance, M.A. (1993). Gene dose of apolipoprotein E type 4 allele and the risk of Alzheimer's disease in late onset families. Science 261, 921–923.

Crowe, E.P., Tuzer, F., Gregory, B.D., Donahue, G., Gosai, S.J., Cohen, J., Leung, Y.Y., Yetkin, E., Nativio, R., Wang, L.-S., et al. (2016). Changes in the transcriptome of human astrocytes accompanying oxidative stress-induced senescence. Front. Aging Neurosci. 8, 208.

Das, U., Scott, D.A., Ganguly, A., Koo, E.H., Tang, Y., and Roy, S. (2013). Activity-induced convergence of APP and BACE-1 in acidic microdomains via an endocytosis-dependent pathway. Neuron 79, 447–460.

De Strooper, B., and Karran, E. (2016). The cellular phase of Alzheimer's disease. Cell 164, 603–615.

Dobin, A., Davis, C.A., Schlesinger, F., Drenkow, J., Zaleski, C., Jha, S., Batut, P., Chaisson, M., and Gingeras, T.R. (2013). STAR: ultrafast universal RNA-seq aligner. Bioinformatics 29, 15–21.

Efthymiou, A.G., and Goate, A.M. (2017). Late onset Alzheimer's disease genetics implicates microglial pathways in disease risk. Mol. Neurodegener. 12, 43.

Fu, H., Liu, B., Frost, J.L., Hong, S., Jin, M., Ostaszewski, B., Shankar, G.M., Costantino, I.M., Carroll, M.C., Mayadas, T.N., and Lemere, C.A. (2012). Complement component C3 and complement receptor type 3 contribute to the phagocytosis and clearance of fibrillar Aβ by microglia. Glia 60, 993–1003.

Goldstein, J.L., DeBose-Boyd, R.A., and Brown, M.S. (2006). Protein sensors for membrane sterols. Cell 124, 35–46.

Göritz, C., Mauch, D.H., Nägler, K., and Pfrieger, F.W. (2002). Role of glia-derived cholesterol in synaptogenesis: new revelations in the synapse-glia affair. J. Physiol. Paris 96, 257–263.

Gosselin, D., Skola, D., Coufal, N.G., Holtman, I.R., Schlachetzki, J.C.M., Sajti, E., Jaeger, B.N., O'Connor, C., Fitzpatrick, C., Pasillas, M.P., et al. (2017). An environment-dependent transcriptional network specifies human microglia identity. Science 356, 6344.

Heslegrave, A., Heywood, W., Paterson, R., Magdalinou, N., Svensson, J., Johansson, P., Öhrfelt, A., Blennow, K., Hardy, J., Schott, J., et al. (2016). Increased cerebrospinal fluid soluble TREM2 concentration in Alzheimer's disease. Mol. Neurodegener. 11, 3.

Holtzman, D.M., Bales, K.R., Wu, S., Bhat, P., Parsadanian, M., Fagan, A.M., Chang, L.K., Sun, Y., and Paul, S.M. (1999). Expression of human apolipoprotein E reduces amyloid-beta deposition in a mouse model of Alzheimer's disease. J. Clin. Invest. 103, R15–R21.

Huang, Y.A., Zhou, B., Wernig, M., and Südhof, T.C. (2017). ApoE2, ApoE3, and ApoE4 differentially stimulate APP transcription and Aβ secretion. Cell 168, 427–441.e21.

Iaccarino, H.F., Singer, A.C., Martorell, A.J., Rudenko, A., Gao, F., Gillingham, T.Z., Mathys, H., Seo, J., Kritskiy, O., Abdurrob, F., et al. (2016). Gamma frequency entrainment attenuates amyloid load and modifies microglia. Nature 540, 230–235.

Keren-Shaul, H., Spinrad, A., Weiner, A., Matcovitch-Natan, O., Dvir-Szternfeld, R., Ulland, T.K., David, E., Baruch, K., Lara-Astaiso, D., Toth, B., et al. (2017). A unique microglia type associated with restricting development of Alzheimer's disease. Cell 169, 1276–1290.e17.

Kim, J., Basak, J.M., and Holtzman, D.M. (2009). The role of apolipoprotein E in Alzheimer's disease. Neuron 63, 287–303.

Koistinaho, M., Lin, S., Wu, X., Esterman, M., Koger, D., Hanson, J., Higgs, R., Liu, F., Malkani, S., Bales, K.R., and Paul, S.M. (2004). Apolipoprotein E promotes astrocyte colocalization and degradation of deposited amyloid-beta peptides. Nat. Med. 10, 719–726.

Lambert, J.C., Ibrahim-Verbaas, C.A., Harold, D., Naj, A.C., Sims, R., Bellenguez, C., DeStafano, A.L., Bis, J.C., Beecham, G.W., Grenier-Boley, B., et al.; European

Alzheimer's Disease Initiative (EADI); Genetic and Environmental Risk in Alzheimer's Disease; Alzheimer's Disease Genetic Consortium; Cohorts for Heart and Aging Research in Genomic Epidemiology (2013). Meta-analysis of 74,046 individuals identifies 11 new susceptibility loci for Alzheimer's disease. Nat. Genet. *45*, 1452–1458.

Langfelder, P., and Horvath, S. (2008). WGCNA: an R package for weighted correlation network analysis. BMC Bioinformatics *9*, 559.

Li, H., and Durbin, R. (2010). Fast and accurate long-read alignment with Burrows-Wheeler transform. Bioinformatics *26*, 589–595.

Liao, F., Hori, Y., Hudry, E., Bauer, A.Q., Jiang, H., Mahan, T.E., Lefton, K.B., Zhang, T.J., Dearborn, J.T., Kim, J., et al. (2014a). Anti-ApoE antibody given after plaque onset decreases Aβ accumulation and improves brain function in a mouse model of Aβ amyloidosis. J. Neurosci. *34*, 7281–7292.

Liao, Y., Smyth, G.K., and Shi, W. (2014b). featureCounts: an efficient general purpose program for assigning sequence reads to genomic features. Bioinformatics *30*, 923–930.

Liu, C.-C., Liu, C.-C., Kanekiyo, T., Xu, H., and Bu, G. (2013). Apolipoprotein E and Alzheimer disease: risk, mechanisms and therapy. Nat. Rev. Neurol. *9*, 106–118.

Liu, Y.-H., Jiao, S.-S., Wang, Y.-R., Bu, X.-L., Yao, X.-Q., Xiang, Y., Wang, Q.-H., Wang, L., Deng, J., Li, J., et al. (2015). Associations between ApoEε4 carrier status and serum BDNF levels—new insights into the molecular mechanism of ApoEε4 actions in Alzheimer's disease. Mol. Neurobiol. *51*, 1271–1277.

Marquer, C., Laine, J., Dauphinot, L., Hanbouch, L., Lemercier-Neuillet, C., Pierrot, N., Bossers, K., Le, M., Corlier, F., Benstaali, C., et al. (2014). Increasing membrane cholesterol of neurons in culture recapitulates Alzheimer's disease early phenotypes. Mol. Neurodegener. *9*, 60.

Masuda, T., Tsuda, M., Yoshinaga, R., Tozaki-Saitoh, H., Ozato, K., Tamura, T., and Inoue, K. (2012). IRF8 is a critical transcription factor for transforming microglia into a reactive phenotype. Cell Rep. *1*, 334–340.

Mathys, H., Adaikkan, C., Gao, F., Young, J.Z., Manet, E., Hemberg, M., De Jager, P.L., Ransohoff, R.M., Regev, A., and Tsai, L.H. (2017). Temporal tracking of microglia activation in neurodegeneration at single-cell resolution. Cell Rep. *21*, 366–380.

Mauch, D.H., Nägler, K., Schumacher, S., Göritz, C., Müller, E.C., Otto, A., and Pfrieger, F.W. (2001). CNS synaptogenesis promoted by glia-derived cholesterol. Science *294*, 1354–1357.

McKenna, A., Hanna, M., Banks, E., Sivachenko, A., Cibulskis, K., Kernytsky, A., Garimella, K., Altshuler, D., Gabriel, S., Daly, M., and DePristo, M.A. (2010). The Genome Analysis Toolkit: a MapReduce framework for analyzing next-generation DNA sequencing data. Genome Res. *20*, 1297–1303.

Mooijaart, S.P., Berbée, J.F.P., van Heemst, D., Havekes, L.M., de Craen, A.J.M., Slagboom, P.E., Rensen, P.C.N., and Westendorp, R.G.J. (2006). ApoE plasma levels and risk of cardiovascular mortality in old age. PLoS Med. *3*, e176.

Muffat, J., Li, Y., Yuan, B., Mitalipova, M., Omer, A., Corcoran, S., Bakiasi, G., Tsai, L.H., Aubourg, P., Ransohoff, R.M., and Jaenisch, R. (2016). Efficient derivation of microglia-like cells from human pluripotent stem cells. Nat. Med. *22*, 1358–1367.

Olsson, A., Venkatasubramanian, M., Chaudhri, V.K., Aronow, B.J., Salomonis, N., Singh, H., and Grimes, H.L. (2016). Single-cell analysis of mixed-lineage states leading to a binary cell fate choice. Nature *537*, 698–702.

Paquet, D., Kwart, D., Chen, A., Sproul, A., Jacob, S., Teo, S., Olsen, K.M., Gregg, A., Noggle, S., and Tessier-Lavigne, M. (2016). Efficient introduction of specific homozygous and heterozygous mutations using CRISPR/Cas9. Nature *533*, 125–129.

Quadrato, G., Nguyen, T., Macosko, E.Z., Sherwood, J.L., Min Yang, S., Berger, D.R., Maria, N., Scholvin, J., Goldman, M., Kinney, J.P., et al. (2017). Cell diversity and network dynamics in photosensitive human brain organoids. Nature *545*, 48–53.

Raja, W.K., Mungenast, A.E., Lin, Y.-T., Ko, T., Abdurrob, F., Seo, J., and Tsai, L.-H. (2016). Self-organizing 3D human neural tissue derived from induced

pluripotent stem cells recapitulate Alzheimer's disease phenotypes. PLoS ONE *11*, e0161969.

Ran, F.A., Hsu, P.D., Wright, J., Agarwala, V., Scott, D.A., and Zhang, F. (2013). Genome engineering using the CRISPR-Cas9 system. Nat. Protoc. *8*, 2281–2308.

Robinson, M.D., McCarthy, D.J., and Smyth, G.K. (2010). edgeR: a Bioconductor package for differential expression analysis of digital gene expression data. Bioinformatics *26*, 139–140.

Robinson, J.T., Thorvaldsdóttir, H., Winckler, W., Guttman, M., Lander, E.S., Getz, G., and Mesirov, J.P. (2011). Integrative genomics viewer. Nat. Biotechnol. *29*, 24–26.

Salter, M.W., and Beggs, S. (2014). Sublime microglia: expanding roles for the guardians of the CNS. Cell *158*, 15–24.

Sarlus, H., and Heneka, M.T. (2017). Microglia in Alzheimer's disease. J. Clin. Invest. *127*, 3240–3249.

Seipel, K., O'Brien, S.P., Iannotti, E., Medley, Q.G., and Streuli, M. (2001). Tara, a novel F-actin binding protein, associates with the Trio guanine nucleotide exchange factor and regulates actin cytoskeletal organization. J. Cell Sci. *114*, 389–399.

Shabalin, A.A. (2012). Matrix eQTL: ultra fast eQTL analysis via large matrix operations. Bioinformatics *28*, 1353–1358.

Shahin, H., Walsh, T., Sobe, T., Abu Sa'ed, J., Abu Rayan, A., Lynch, E.D., Lee, M.K., Avraham, K.B., King, M.-C., and Kanaan, M. (2006). Mutations in a novel isoform of TRIOBP that encodes a filamentous-actin binding protein are responsible for DFNB28 recessive nonsyndromic hearing loss. Am. J. Hum. Genet. *78*, 144–152.

Shi, Y., Yamada, K., Liddelow, S.A., Smith, S.T., Zhao, L., Luo, W., Tsai, R.M., Spina, S., Grinberg, L.T., Rojas, J.C., et al.; Alzheimer's Disease Neuroimaging Initiative (2017). ApoE4 markedly exacerbates tau-mediated neurodegeneration in a mouse model of tauopathy. Nature *549*, 523–527.

Sidoryk-Wegrzynowicz, M., Wegrzynowicz, M., Lee, E., Bowman, A.B., and Aschner, M. (2011). Role of astrocytes in brain function and disease. Toxicol. Pathol. *39*, 115–123.

Strittmatter, W.J., Saunders, A.M., Schmechel, D., Pericak-Vance, M., Enghild, J., Salvesen, G.S., and Roses, A.D. (1993). Apolipoprotein E: high-avidity binding to beta-amyloid and increased frequency of type 4 allele in late-onset familial Alzheimer disease. Proc. Natl. Acad. Sci. USA *90*, 1977–1981.

Subramanian, A., Tamayo, P., Mootha, V.K., Mukherjee, S., Ebert, B.L., Gillette, M.A., Paulovich, A., Pomeroy, S.L., Golub, T.R., Lander, E.S., and Mesirov, J.P. (2005). Gene set enrichment analysis: a knowledge-based approach for interpreting genome-wide expression profiles. Proc. Natl. Acad. Sci. USA *102*, 15545–15550.

Theendakara, V., Peters-Libeu, C.A., Spilman, P., Poksay, K.S., Bredesen, D.E., and Rao, R.V. (2016). Direct transcriptional effects of Apolipoprotein E. J. Neurosci. *36*, 685–700.

Toh, W.H., and Gleeson, P.A. (2016). Dysregulation of intracellular trafficking and endosomal sorting in Alzheimer's disease: controversies and unanswered questions. Biochem. J. *473*, 1977–1993.

Trapnell, C., Roberts, A., Goff, L., Pertea, G., Kim, D., Kelley, D.R., Pimentel, H., Salzberg, S.L., Rinn, J.L., and Pachter, L. (2012). Differential gene and transcript expression analysis of RNA-seq experiments with TopHat and Cufflinks. Nat. Protoc. *7*, 562–578.

Ulrich, J.D., and Holtzman, D.M. (2016). TREM2 function in Alzheimer's disease and neurodegeneration. ACS Chem. Neurosci. *7*, 420–427.

Wang, K., Li, M., and Hakonarson, H. (2010). ANNOVAR: functional annotation of genetic variants from high-throughput sequencing data. Nucleic Acids Res. *38*, e164.

Wang, C., Najm, R., Xu, Q., Jeong, D.E., Walker, D., Balestra, M.E., Yoon, S.Y., Yuan, H., Li, G., Miller, Z.A., et al. (2018). Gain of toxic apolipoprotein E4 effects in human iPSC-derived neurons is ameliorated by a small-molecule structure corrector. Nat. Med. https://doi.org/10.1038/s41591-018-0004-z.

Wyss-Coray, T., Loike, J.D., Brionne, T.C., Lu, E., Anankov, R., Yan, F., Silverstein, S.C., and Husemann, J. (2003). Adult mouse astrocytes degrade amyloid-beta in vitro and in situ. Nat. Med. 9, 453–457.

Xu, Q., Bernardo, A., Walker, D., Kanegawa, T., Mahley, R.W., and Huang, Y. (2006). Profile and regulation of apolipoprotein E (ApoE) expression in the CNS in mice with targeting of green fluorescent protein gene to the ApoE locus. J. Neurosci. 26, 4985–4994.

Zhang, Y., Liu, T., Meyer, C.A., Eeckhoute, J., Johnson, D.S., Bernstein, B.E., Nusbaum, C., Myers, R.M., Brown, M., Li, W., and Liu, X.S. (2008). Model-based analysis of ChIP-seq (MACS). Genome Biol. 9, R137.

Zhang, Y., Pak, C., Han, Y., Ahlenius, H., Zhang, Z., Chanda, S., Marro, S., Patzke, C., Acuna, C., Covy, J., et al. (2013). Rapid single-step induction of functional neurons from human pluripotent stem cells. Neuron 78, 785–798.

Zhang, L., Fang, Y., Lian, Y., Chen, Y., Wu, T., Zheng, Y., Zong, H., Sun, L., Zhang, R., Wang, Z., and Xu, Y. (2015). Brain-derived neurotrophic factor ameliorates learning deficits in a rat model of Alzheimer's disease induced by aβ1-42. PLoS ONE 10, e0122415.

Zhang, Y., Sloan, S.A., Clarke, L.E., Caneda, C., Plaza, C.A., Blumenthal, P.D., Vogel, H., Steinberg, G.K., Edwards, M.S.B., Li, G., et al. (2016). Purification and characterization of progenitor and mature human astrocytes reveals transcriptional and functional differences with mouse. Neuron 89, 37–53.

Zhao, J., Davis, M.D., Martens, Y.A., Shinohara, M., Graff-Radford, N.R., Younkin, S.G., Wszolek, Z.K., Kanekiyo, T., and Bu, G. (2017). APOE ε4/ε4 diminishes neurotrophic function of human iPSC-derived astrocytes. Hum. Mol. Genet. 26, 2690–2700.

STAR★METHODS

KEY RESOURCES TABLE

REAGENT or RESOURCE	SOURCE	IDENTIFIER
Antibodies		
Rabbit monoclonal anti-Aβ (D54D2)	Cell Signaling Technology	Cat#8243
Rabbit monoclonal anti-APOE (clone EP1374Y)	Abcam	Cat#AB52607, RRID: AB_2258476
Mouse monoclonal anti-p-tau (clone AT-8)	Thermo Fisher Scientific	Cat#MN1020, RRID: AB_223647
Rat monoclonal anti-CD11b-APC	Miltenyi Biotec	Cat#130-091-241, RRID: AB_244268
Mouse monoclonal anti-EEA1	BD Transduction Laboratiories	Cat#610457, RRID: AB_397830
Mouse monoclonal anti-GAPDH (clone 6C5)	Santa Cruz Biotechnology	Cat#SC-32233, RRID: AB_627679
Rabbit polyclonal anti-GFAP	Millipore	Cat#AB5804, RRID: AB_2109645
Mouse monoclonal anti-GLAST-PE	Mitenyi Biotec	Cat#130-098-804, RRID: AB_2660782
Rabbit monoclonal anti-Iba1	Wako Chemicals	Cat#019-19471, RRID: AB_2665520
Goat polyclonal anti-Iba1	Novus Biologicals	Cat# NB 100-1028, RRID: AB_521594
Chichen polyclonal anti-MAP2	BioLegend	Cat#822501, RRID: AB_2564858
Rabbit polyclonal anti-Nestin	Millipore	Cat#AB91107, RRID: AB_91107
Rabbit polyclonal anti-PSD-95	Abcam	Cat#AB18258, RRID: AB_444362
Rabbit polyclonal anti-PSD-95	Cell Signaling Technology	Cat# 3450S, RRID: AB_2292883
Mouse monoclonal anti-S100β	Sigma-Aldrich	Cat#AMAB91038, RRID: AB_2665776
Goat polyclonal anti-SOX2 (clone Y-17)	Santa Cruz Biotechnology	Cat#SC-17320, RRID: AB_2286684
Mouse monoclonal anti-Synaptophysin (clone SVP-38)	Sigma-Aldrich	Cat#S5768, RRID: AB_477523
Mouse polyclonal anti-TRA-1-60	Stemgent	Cat#09-0068, RRID: AB_2233143
Rabbit monoclonal anti-TREM2 (clone D814C)	Cell Signaling Technology	Cat#91068, RRID: AB_2721119
Rabbit monoclonal anti-IDE	Abcam	Cat#AB133561
Mouse monoclonal anti-β-actin	Sigma-Aldrich	Cat# A5441, RRID: AB_476744
Chemicals, Peptides, and Recombinant Proteins		
Apolipoprotein E4 human	Sigma-Aldrich	Cat#A3234
Apolipoprotein E3 human	Sigma-Aldrich	Cat#SRP4696
Beta-Amyloid (1-42), Human	Anaspec	Cat#AS-20276
Beta-Amyloid (1-42) HiLyte Fluor555-labeled, Human	Anaspec	Cat#AS-60480-01
Leupeptin	Sigma-Aldrich	Cat#L2884
Chloroquine diphosphate salt	Sigma-Aldrich	Cat#C6628
Ammonium chloride	Sigma-Aldrich	Cat#A9434
Critical Commercial Assays		
Amyloid beta 40 Human ELISA Kit	Thermo Fisher Scientific	Cat#KHB3482
Amyloid beta 42 Human ELISA Kit	Thermo Fisher Scientific	Cat#KHB3442
Cholesterol Assay Kit (cell-based)	Abcam	Cat#AB133116
Cholesterol Assay Kit - HDL and LDL/VLDL	Abcam	Cat#AB65390
CellTiter-Glo Luminescent Cell Viability Assay	Promega	Cat#G7570
Deposited Data		
Raw data lifes for RNA-seq	This paper	GEO: GSE102956
Experimental Models: Cell Lines		
Human induced-pluripotent stem cell line_AG09173	Coriell	Cat#AG09173
Human induced-pluripotent stem cell line_AG10788	Coriell	Cat#AG10788

(Continued on next page)

Continued

REAGENT or RESOURCE	SOURCE	IDENTIFIER
Oligonucleotides		
APOE sgRNA oligomer pair (Forward): 5′-CACCGC CTCGCCGCGGTACTGCACC-3′	This paper	N/A
APOE sgRNA oligomer pair (Reverse): 5′-AAACGG TGCAGTACCGCGGCGAGGC-3′	This paper	N/A
ssODN for *APOE3* -> *APOE4*: 5′- GAGGAGACGC GGGCACGGCTGTCCAAGGAGCTGCAGGCGGC GCAGGCCCGGCTGGGCGCGGACATGGAGGA CGTGCGCGGCCGGCTGGTGCAGTACCGCGGC GAGGTGCAGGCCATGCTCGGCCAGAGCACCG AGGAGCTGCGGGTGCGCCTCGCCTCCCACCT GCGCAAGCTGCGTAAG-3′	This paper	N/A
ssODN for *APOE4* -> *APOE3*: 5′- GAGGAGACGC GGGCACGGCTGTCCAAGGAGCTGCAGGCGGC GCAGGCCCGGCTGGGCGCGGACATGGAGGAC GTGTGCGGCCGGCTGGTGCAGTACCGCGGCG AGGTGCAGGCCATGCTCGGCCAGAGCACCGA GGAGCTGCGGGTGCGCCTCGCCTCCCACCTG CGCAAGCTGCGTAAG −3′	This paper	N/A
Recombinant DNA		
pSpCas9(BB)-2A-GFP (PX458)	Addgene	Cat#48138
FUdeltaGW-rtTA	Addgene	Cat#19780
pLV-TetO-hNGN2-eGFP-Puro	Südhof lab	N/A
pRSV-Rev	Addgene	Cat#12253
pCMV-VSV-G	Addgene	Cat#8545
Software and Algorithms		
ImageJ	NIH	https://imagej.nih.gov/ij/index.html
Prism	GraphPad	https://www.graphpad.com/scientific-software/prism/
IMARIS	Bitplane	http://www.bitplane.com/imaris
STAR	Gingeras Lab	http://labshare.cshl.edu/shares/gingeraslab/www-data/dobin/STAR
CUFFLINKS	Trapnell Lab	http://cole-trapnell-lab.github.io/cufflinks/

CONTACT FOR REAGENT AND RESOURCE SHARING

Further information and requests for resources and reagents should be directed to and will be fulfilled by the Lead Contact, Li-Huei Tsai (lhtsai@mit.edu).

EXPERIMENTAL MODEL AND SUBJECT DETAILS

Human induced-pluripotent stem cells
Unaffected (Coriell #AG09173, female, Age 75) and sporadic AD (Coriell #AG10788, female, Age 87) iPSC lines have been fully characterized and the *APOE* genotype was confirmed by sequencing. iPSCs were cultured on irradiated mouse embryonic fibroblasts (MEFs, MTI-GlobalStem) in human ES (hES) media [DMEM/F12, HEPES media (GIBCO) supplemented with 20% knockout serum replacement (KSR) (GIBCO), 1X non-essential amino acids (NEAA), 1X GlutaMAX, (Life Technologies), 12 nM beta-fibroblast growth factor (FGF2, PeproTech) and 0.1 mM 2-mercaptoethanol (Sigma-Aldrich)]. iPSCs were maintained at 37°C and 5% CO_2 in a humidified incubator.

METHOD DETAILS

Generation of isogenic iPSC lines
Preparation of the CRISPR/Cas9-ApoE sgRNA plasmid
We prepared CRISPR/Cas9-*APOE* sgRNA plasmid following published protocol published (Ran et al., 2013). Briefly, we designed a sgRNA sequence (5′-CCTCGCCGCGGTACTGCACC-3′) within 10 nucleotides from the target site corresponding to amino acid 112

using the CRISPR Design tool (http://crispr.mit.edu). We annealed the oligomer pairs (5′-CACCGCCTCGCCGCGGTACTGCACC-3′ and 5′-AAACGGTGCAGTACCGCGGCGAGGC-3′) and cloned them into pSpCas9-2A-GFP (PX458) plasmid (Addgene #48138). Plasmid DNA was submitted for Sanger sequencing to confirm correct *APOE* sgRNA sequence. We also designed single-strand oligo-deoxynucleotides (ssODN) to convert *APOE4* to *APOE3*, or *APOE3* to *APOE4* with a silent mutation at the protospacer adjacent motif (PAM) site to prevent recurrent Cas9 cutting in edited cells.: *APOE3 -> APOE4*: GAGGAGACGCGGGCACGGCTGTCCAAGGAGCTGC AGGCGGCGCAGGCCCGGCTGGGCGCGGACATGGAGGACGTGCGCGGCCGGCTGGTGCAGTACCGCGGCGAGGTGCAGGCCA TGCTCGGCCAGAGCACCGAGGAGCTGCGGGTGCGCCTCGCCTCCCACCTGCGCAAGCTGCGTAAG; *APOE4 -> APOE3*:GAGGA GACGCGGGCACGGCTGTCCAAGGAGCTGCAGGCGGCGCAGGCCCGGCTGGGCGCGGACATGGAGGACGTGTGCGGCCGGCT GGTGCAGTACCGCGGCGAGGTGCAGGCCATGCTCGGCCAGAGCACCGAGGAGCTGCGGGTGCGCCTCGCCTCCCACCTGCGC AAGCTGCGTAAG.

Electroporation
iPSCs with 70 to 80% confluence were dissociated by treating with accutase (Thermo Fisher Scientific) and 10 μM ROCK inhibitor (Tocris) for 20 min. After spinning down iPSCs at 160 x *g* for 3 min, the number of cells was counted and 5 million cells were subjected to electroporation. Electroporation was performed using Nucleofector – Amaxa and Human Stem Cell Nucleofector Kit 1(Lonza) according to the manufacturer's instructions. In brief, cells were resuspended in 100 μl of reaction buffer from the kit and 7.5 μg of CRISPR/Cas9-*APOE* sgRNA plasmid and 15 μg of ssODN were added to cell suspension. After electroporation with A-23 protocol, we resuspended cells with hES media with 10 μM ROCK inhibitor and seeded them onto plates containing MEFs.

Fluorescence-activated cell sorting (FACS)
Two days after electroporation, we performed FACS to isolate GFP-expressing iPSCs. Briefly, dissociated cells using accutase/ROCK inhibitor for 20 min were washed and resuspended with DPBS. Then, cells were filtered using Falcon polystyrene test tubes (#352235, Corning) and transferred to Falcon polypropylene test tubes (#352063, Corning). Sorting was performed by BD FACSAria IIU in FACS Facility at the Whitehead Institute. Sorted cells were suspended in recovery medium [hES medium with 1X Penicillin-Streptomycin (P/S) (Gemini Bio-products) and ROCK inhibitor] and plated onto 6-well plates containing MEFs (50K cells/well).

Colony inspection
Each colony was transferred to one well of 12-well plate coated with MEFs and maintained until the colony grew big enough to be transferred to another 12-well plate. After the second transfer, iPSCs in the original plate were dissociated and genomic DNA was extracted. Primers (5′-CTGGAGGAACAACTGACCCC-3′ and 5′-CTCGAACCAGCTCTTGAGGC-3′) were used to amplify DNA in *APOE* gene and PCR products were submitted to GENEWIZ for Sanger sequencing.

Karyotyping
In order to identify and evaluate the size, shape, and number of chromosomes in iPSCs, we performed karyotyping after colony inspection. iPSCs were cultured on hESC-qualified matrigel (Corning) coated T25 cell culture flasks in mTeSR1 media (STEMCELL Technologies) until 60% confluence, and then sent to Cell Line Genetics for karyotyping.

Differentiation of iPSCs into neurons
We generated excitatory neurons from iPSCs according to published protocol (Zhang et al., 2013). Briefly, iPSCs were prepared on matrigel coated 6-well plates at a density of 4×10^6 cells/well. Two hours later, lentivirus with rtTA and Ngn2-GFP expression vectors were suspended in mTeSR1 media with 2 μM thiazovivin (Tocris) and added to the iPSCs plates. After 24 hr, the culture medium was fully changed with N2(1X)/DMEM/F12/NEAA(1X) (Thermo Fisher Scientific) medium containing 10 ng/ml BDNF (Peprotech), 10 ng/ml NT-3 (Peprotech), 0.2 μg/ml laminin (Corning), and 2 μg/ml doxycycline (Sigma-Aldrich) to induce TetO gene expression. The following day, old media was removed and replaced with Neurobasal/B27(1X)/GlutaMAX(1X) (Thermo Fisher Scientific) medium containing 10 ng/ml BDNF, 10 ng/ml NT-3, 0.2 μg/ml laminin, 2 μg/ml doxycycline and 1 μg/ml puromycin (Millipore). Two days after puromycine treatment, Ngn2-GFP expressing cells were purified by FACS and plated onto matrigel-coated plates containing human astrocyte (ScienCell, #1850) in conditioned medium containing 10 ng/ml BDNF, 10 ng/ml NT-3, 0.2 μg/ml laminin, 2 μg/ml doxycycline, and 1 μg/ml puromycin. The next day, 1 μM Ara-C (Sigma-Aldrich) was added to cultured media. Three days after Ara-C treatment, media was removed and replaced with astrocyte conditioned medium containing 10 ng/ml BDNF, 10 ng/ml NT-3, 0.2 μg/ml laminin and 0.5 μg/ml doxycycline. One half plate volume of media was replaced with new media every 4 days until the cells were ready for experimental assays.

Differentiation of iPSCs into astrocytes
iPSCs were cultured in 6-well plate coated with hESC-qualified matrigel (Corning) in mTeSR1 media until cells had reached ~100% confluence. Then, cells were washed with DPBS and 2 mL of neural induction media [1:1 mixture of N-2 (DMEM/F-12 GlutaMAX, 1X N-2, 5 μg/ml insulin, 1 X NEAA, 100 μM 2-mercaptoethanol, and 1X P/S) and B-27 (Neurobasal medium, 1X B-27, 1X GlutaMAX, and 1X P/S media)] were added. Cells were treated with 1 μM Dorsomorphin and 10 μM SB431542 for 12 days, then passaged to new matrigel coated plates using accutase. Cells were cultured in neural maintenance media until the neural rosette structures became visible under the microscope (around days 16-24). Then, cells were passaged again with accutase and seeded at 4×10^6 cells/well density into matrigel coated 6-well plate. The day after passage, 20 ng/ml FGF2 (Peprotech) and 10 ng/ml BMP4 (Peprotech) were added into neural maintenance media. Media was changed every other day for 28 days and FACS were performed using GLAST antibody (Miltenyi Biotec) to purify astrocytes. After sorting, cells were seeded at 2.5×10^5 cells/well density into 6-well plate and

cultured in astrocyte media (Sciencell) every other day for 7 days. After 7 days, we performed FACS with GLAST antibody again to increase the purity of astrocyte cultures. These cells were used for all experiments.

Generation of induced microglia-like cells

We derived microglia-like cells from iPSCs as previously described (Muffat et al., 2016). Briefly, iPSCs on MEFs-coated plates were dissociated with Collagenase IV (Thermo Fisher Scientific). iPSCs were then resuspended in MGD media [Neurobasal media supplemented with 0.5X Gem21 (Gemini Bio-products), 0.5X Neuroplex N2 (Gemini Bio-products), 0.2% Albumax I (Thermo Fisher Scientific), 5 mM sodium chloride (Sigma-Aldrich), 1X sodium pyruvate, 1X P/S, 1X GlutaMAX, 3.5 ng/ml biotin (Sigma-Aldrich), 10 μM ascorbic acid (Sigma-Aldrich) and 1.7% lactic syrup (Sigma-Aldrich)] with 10 ng/ml IL-34 (Peprotech) and 10 ng/ml M-CSF1(Peprotech)], and cultured in ultra-low attachment 6-well plates (Corning). Once the phase-bright neutralized spheroids and cystic bodies appeared, Embryoid bodies were gently triturated to shear off cells of interest, and supernatants were transferred to a single well of Primaria 6-well plate (Corning). Attached cells showed morphological characteristics of microglia and microglia precursors. Cells from 6 consecutive productions were pooled and purified by FACS using CD11b antibody (Miltenyi Biotec). Collected cells were further maintained in MGD media with 100 ng/ml IL-34 and 5 ng/ml M-CSF for all experiments.

Organoids culture

We derived organoids according to our published protocol (Raja et al., 2016). Briefly, iPSCs were maintained on MEFs until 80% confluence and dissociated using accutase. Then, cells were plated onto 0.1% gelatin (Millipore) coated 10 cm dish (Falcon) for 45min and non-adherent iPSCs were collected and seeded at a density of 1.2×10^4 cells/well into V-shape 96-well plates (VWR) pre-coated with 1% pluronic acid (Sigma-Aldrich). Cells were maintained for 18 days in media consisted of Glasgow-MEM (Thermo Fisher Scientific) with 20% KSR, 1X sodium pyruvate, 1X NEAA, 0.1 mM 2-mercaptoethanol, 20 μM Rock inhibitor, 5 μM SB431532 (Tocris), and 3 μM IWRe1 (Tocris). Dorsomorphin (2 μM, Tocris) was added to media after the first three days. Media was changed every other day for 18 days and then organoids were transferred to non-adherent EZsphere dishes (Nacalai USA). At day 18, organoids were cultured in media with DMEM/F12 supplemented with 1X Chemically Defined Lipid Concentrate (Thermo Fisher Scientific) and 1X N2-supplement in an incubator (5% CO_2 and 40% O_2). At day 35, 5 μM heparin (Sigma-Aldrich), 10% FBS (Gemini Bio-products) and 1% matrigel (Corning) were added to media until day 70. At day 70, the concentration of matrigel was increased to 2% and 1X B27 supplement was added for the remainder of the culture period. Media in the dishes was changed every 4 to 5 days.

Bioinformatics

Genomic variant analysis for genome-edited iPSCs

Exome-seq data (76-bp paired-end) were generated at the sequencing core facility of the Broad Institute of MIT & Harvard. Our data processing pipeline was established based on "GATK Best Practices" recommended by Broad GATK team. Briefly, the raw fastq files were first mapped to human hg19 assembly using BWA mapper (version 7, mem option) (Li and Durbin, 2010); PCR duplicates were removed using MarkDuplicates function of Picard software package (http://broadinstitute.github.io/picard/). RealignerTargetCreator, IndelRealigner and BaseRecalibrator modules of GATK tools (McKenna et al., 2010) were further employed to perform local realignment and recalibration. HaplotypeCaller of GATK tools was then used to call variants in exonic regions with stand_emit_conf of 10 and stand_call_conf of 30. SNP and INDEL variants were selected using SelectVariants of GATK tools. Genomic variants from genome-edited iPSCs were compared to the variants from their parental lines to identify unique variants to genome-edited iPSCs. Further removal of variants overlapping with repeatmasker regions and variants with low DP and QUAL scores were carried out before functional annotation of exonic variants using ANNOVAR package (Wang et al., 2010). All potential unique variants identified from the above variant calling pipeline were finally examined manually by overlaying bam traces of genome-edited iPSCs with their parental lines in IGV browser (Robinson et al., 2011).

RNA-seq analysis of iPSC-derived cell lines

Extracted total RNA was subject to QC using an Advanced Analytical-fragment Analyzer before library preparation using Illumina Neoprep stranded RNA-seq library preparation kit. Libraries were pooled for sequencing using Illumina HiSeq2000 or NextSeq500 platforms at the MIT Biomicro Center. The raw fastq data were aligned to human hg19 assembly using STAR 2.4.0 RNA-seq aligner (Dobin et al., 2013). Mapped RNA-seq reads covering the edited *APOE3/4* site were used to validate data genotypes. Gene raw counts were generated from the mapped data using featureCounts tool (Liao et al., 2014b). The mapped reads were also processed by Cufflinks2.2 (Trapnell et al., 2012) with hg19 reference gene annotation to estimate transcript abundances. Gene differential expression test between *APOE3* and *APOE4* groups of each cell type was performed using Cuffdiff module with adjusted q-value < 0.05 for statistical significance. Geometric method was chosen as the library normalization method for Cuffdiff. Color-coded scatterplots were used to visualize group FPKM values for differentially expressed genes and other genes.

Gene raw count matrix was processed by edgeR package (Robinson et al., 2010) to generate logCPM values (CPM – counts per million) for data clustering analysis. Phylogenetic tree was constructed based on Euclidean distance of logCPM values of group average count values and ward.D2 option of hclust tool. Correlation heatmap was generated using replicate logCPM matrix combed with data matrix of publicly available iPSC-derived neuron/microglia RNA-seq data (Busskamp et al., 2014; Muffat et al., 2016) and human fetal brain astrocyte RNA-seq data (Crowe et al., 2016). In the correlation heatmap, the correlation matrix was reordered based on average linkage hierarchical clustering with rectangular boxes to visualize sample clusters. Z-scores of replicate expression

FPKM values for differentially expressed genes were visualized in heatmaps for different cell types. Gene ontology was performed using Broad GSEA tool (Subramanian et al., 2005) and TOPPGENE tool (Chen et al., 2009).

Gene co-expression network analysis

Weighted gene co-expression network analysis (WGCNA) (Langfelder and Horvath, 2008) was applied to explore gene co-expression pattern in iPSC-derived brain cell types. Briefly, raw count data from 26 RNA-seq samples were processed by edgeR to generate logCPM matrix before calculating a set of soft-thresholding powers for signed network construction. A power value of 10 (SFT.R.sq > 0.8, approximately scale-free) was chosen to compute adjacency matrix for a signed co-expression network. The topological overlap matrix (TOM) was then calculated, and average linkage hierarchical clustering was used to group genes based on their topological overlap. A dynamic tree-cutting method was used (minClusterSize = 100 and cutHeight = 0.999) to create gene co-expression modules and the results were visualized in a dendrogram.

GWAS analysis of human brain exome-seq data and eQTL analysis of human brain RNA-seq data

Human brain (normal control and mild cognitive impairment subjects) exome-seq and RNA-seq data were collected from NIH-AMP/AD consortium. Those data were generated from postmortem brain tissue collected through the Mount Sinai VA Medical Center Brain Bank and were provided by Dr. Eric Schadt from Mount Sinai School of Medicine. From 341 exome-seq data, a total of 117,132 SNPs and INDELs were reported within exome-seq covered regions. Further trait association was performed using Matrix_eQTL tool (Shabalin, 2012) to associate genomic variants with mean neocortical plaque density value (race and gender as covariates). The calculated p values were visualized in a Manhattan plot. Variants with p value less than 1×10^{-5} were subject to further functional annotation with ANNOAR. Normalized gene count matrix for 880 RNA-seq data generated from postmortem brain in four different areas (BM10, BM22, BM36, BM44) were filtered to get expression matrices for genes specifically expressed in neurons, microglia or astrocytes. Cell specific gene sets were defined based on Dr. Ben Barres' human adult brain cell-type specific RNA-seq data (Zhang et al., 2016) with a cutoff of 2-fold higher expression in a particular cell type than any other cell type. Expression matrices for cell specific gene sets were then used to examine variation of gene expression associated with *APOE4* homozygous mutation by Matrix_eQTL (calculation of effect size β and statistical p value). In parallel, expression fold change and statistical p value between *APOE3* and *APOE4* groups for cell specific genes in iPSC-derived corresponding cell types were collected for comparison with human brain data. Scatterplots of fold change versus effect size for neuronal, microglial and astrocytic genes were generated with statistically significance (p < 0.05 for both data) coded by different colors. Spearman's correlation analysis of gene expression with pathological plaque density and clinical dementia rating (CDR) was performed using customized R scripts. Heatmaps were generated using combined information of correlation rho value and statistical p value. Spearman's rho value and p value were calculated using Spearman's rank correlation test, which assesses relationships of ordinal variables.

Aggregation plot of average Irf8 ChIP-Seq intensity signals around gene transcription start sites

With One set of Irf8 ChIP-Seq data (GEO: GSE70237) produced in mouse bone marrow (so the cell types could be considered as similar to our microglia-like cells; Olsson et al., 2016), we performed ChIP-Seq analysis using MACS2 software tool (Zhang et al., 2008) to generate fold enrichment of Irf8 against input across the entire mouse genome. The up and downregulated genes (DEGs - differentially expressed genes) in *APOE4* microglia-like cells compared to *APOE3* microglia-like cells were converted to the mouse orthologs, and enriched Irf8 ChIP-Seq signals around the transcription start sites of DEGs were aggregated for visualization.

Immunoblot analysis

iPSC-derived brain cell types or organoids were collected in 1.5 mL tubes and washed three times with DPBS. The samples were then lysed with RIPA buffer (50 mM Tris, pH 8.0, 150 mM NaCl, 1% NP40, 0.5% sodium deoxycholate, 0.1% SDS) containing protease and phosphatase inhibitors. Lysates were spun at 13,000 rpm for 15 min and only supernatants were transferred to new tubes. Protein concentration of samples was measured (Bio-Rad Protein Assay) and equal amount of protein was loaded for electrophoresis.

Immunostaining analysis

Neurons and glial cells

After growing on glass coverslips, cells were washed three times with DPBS and fixed with 4% paraformaldehyde in PBS for 15min. After fixation, cells were washed with DBPS and permeabilized with blocking solution containing 0.1% Triton X-100, 10% donkey serum, 2% BSA and 1 M glycine in PBS for 1hr at room temperature. Then cells were incubated with appropriate antibodies overnight at 4°C. The following day, cells were incubated with fluorescently conjugated secondary antibodies (Molecular Probes) and Hoechst 33342 (Invitrogen) for 1hr at room temperature and washed three times with DPBS before mounting on the glass slide. For the quantification of synaptophysin and PSD-95 puncta in iPSC-derived neurons, IMARIS software (Bitplane) was used. The path of process was generated based on PSD-95 signals with the filaments module and puncta were marked based on the threshold we set (For synaptophysin, surface area detail level was set to 0.5 μM, and intensity threshold with background subtraction was set to 1.0 μM / for PSD-95, surface area detail levels to 0.25 μM, and intensity threshold with background subtraction to 0.5 μM). Marked puncta then digitalized for the quantification.

Organoids

After culturing in incubator for three months or six months, organoids were washed three times with DPBS and fixed with 4% para-formaldehyde in PBS for 15min. After fixation, organoids were dehydrated with 30% sucrose in PBS at 4°C. Organoids were then

embedded with Optical cutting temperature (OCT) compound (VWR) and frozen by dry ice. The frozen block with organoids were sectioned at −20°C using cryosection with 20 μm thickness and transferred to the glass slide. Organoid samples on the glass slide were washed with DBPS and permeabilized with blocking solution containing 0.1% Triton X-100, 10% donkey serum, 2% BSA and 1 M glycine in PBS for 1hr at room temperature. Then samples were incubated with appropriate antibodies overnight at 4°C. Next day, samples were incubated with fluorescently conjugated secondary antibodies and Hoechst 33342 for 1hr at room temperature and washed three times with PBS before mounting with the glass coverslip.

Electrophysiology
Six weeks old iPSC-derived neurons were subjected for whole cell recording to measure miniature excitatory postsynaptic currents (mEPSCs). The external solution consists of 130 mM NaCl, 4 mM KCl, 2 mM $CaCl_2$, 1 mM $MgCl_2$, 10 mM HEPES and 10 mM glucose (pH = 7.4). TTX (1 μM) and picrotoxin (50 μM) were added to block spontaneous firing and GABA-mediated currents. EGFP-positive neurons were held at −70 mV with recording pipettes containing 145 mM CsCl mM, 5 NaCl mM, 10 HEPES-CsOH mM, 10 EGTA mM, 4 MgATP mM and 0.3 mM Na_2GTP. Recording was performed using an Axoclamp 200B amplifier with a Digidata 1440A A-D converter (Axon Instruments), and all data were analyzed by the use of pClamp 10 software (Axon Instruments).

Synaptophysin puncta quantification in iPSC-derived neurons
Dendritic branches 40 μm away from cell body were subjected for data analysis. In branches, only synaptophysin puncta within 2 μm from PSD-95 signals were quantified.

Measurement of secreted Aβ levels in iPSC-derived neurons by ELISA
iPSC-derived neurons were prepared in 96-well plates. After six weeks of differentiation, media was fully changed and kept for two days. Then, media were collected and secreted Aβ levels were measured using human $A\beta_{42}$ or $A\beta_{40}$ ELISA kit.

Cholesterol assay
Cholesterol levels in iPSC-derived astrocytes or astrocyte cultured media were measured using cholesterol assay kits (Abcam) following the manufacturer's instructions. For the measurement of cholesterol levels in astrocyte, cells were plated on glass coverslips. Astrocytes were washed three times with DPBS and fixed with 4% paraformaldehyde in PBS for 15min. Cells were treated with filipin III for 1hr and washed with DPBS. Fluorescence from cholesterol-bound filipin III was detected by microplate reader (EnSpire, Perkin Elmer), microscope or FACS. To measure secreted cholesterol levels in iPSC-derived astrocytes, cells were prepared in 24-well plates. The day after passaging, media were fully changed. Two days later, media were collected and secreted cholesterol levels were measured using an EnSpire plate reader (Perkin Elmer).

Microscopy
All images were captured using Zeiss LSM 710 confocal microscope and Zen software, and analyzed using ImageJ (National Institutes of Health) or IMARIS software.

$A\beta_{42}$ uptake assay
iPSC-induced astrocytes
To prepare oligomerized $A\beta_{42}$, $A\beta_{42}$ peptide (AnaSpec) was dissolved in 1% NH_4OH at 1 mg/ml and sonicated. Lyophilized $A\beta_{42}$ was further dissolved in water, filtered and incubated at 37°C for 1 day before use. iPSC-derived astrocytes were seeded in 24-well plates (3×10^4 /well) for 2 days and incubated with oligomeric $A\beta_{42}$ (250 ng/ml) for additional 2 days. $A\beta_{42}$ oligomer was also added to media only (without cells) to measure total levels of $A\beta_{42}$ 2 days after culture. The levels of $A\beta_{42}$ in cultured media 2 days after treatment were measured by human $A\beta_{42}$ ELISA kit (Invitrogen) following the manufacturer's instructions. Reduced levels of $A\beta_{42}$ by iPSC-derived astrocytes were calculated by subtracting remaining $A\beta_{42}$ from total $A\beta_{42}$. $A\beta_{42}$ uptake index was obtained from dividing reduced levels of $A\beta_{42}$ by the number of cells measured by CellTiter-Glo cell viability assay (Promega).
Induced microglia-like cells
For imaging $A\beta_{42}$ uptake by microglia-like cells, $A\beta_{42}$ labeled with HiLyte Fluor-555 peptide (AnaSpec) was used. The peptide was dissolved in 1% NH_4OH at 10 mg/ml and further diluted with PBS at 1 mg/ml. Microglia-like cells were seeded at (2×10^4 /well) for 2 days before the experiment. Microglia-like cells were treated with $A\beta_{42}$-555 (1 μg/ml) for 1hr for live imaging. Time series experiments consisted of sixty 512x512 frames with an interval of 1min. Image stacks were exported to ImageJ, and fluorescence intensities were measured.

Lysosomal inhibitors treatment in iPSC-derived astrocytes
iPSC-derived astrocytes were prepared in 6-well plates. The day after passaging, media was fully changed and incubated with lysosomal inhibitors [leupeptin (50 μM), chloroquine (50 μM) and ammonium chloride (10 mM) for 48 hr. Cells were washed with DPBS three times and lysed with RIPA buffer containing protease and phosphatase inhibitors. Lysates were spun at 13,000 rpm for 15min and only supernatants were transferred to new tubes.

QUANTIFICATION AND STATISTICAL ANALYSIS

Statistical analyses

Statistical analyses were performed using Prism 6 (GraphPad Software). ANOVAs followed by Tukey's test, Dunnett's test or unpaired Student's t tests were used. All data are represented as mean ± s.e.m.

DATA AND SOFTWARE AVAILABILITY

The accession number for the RNA-seq data reported in this paper is GEO: GSE102956.